Earth pressure in narrow cohesive-fictional soils behind retaining walls rotated about the top

An analytical approach

Yang, Dayu; Lai, Fengwen; Liu, Songyu

DOI
10.1016/j.compgeo.2022.104849

Publication date
2022

Document Version
Final published version

Published in
Computers and Geotechnics

Citation (APA)
Yang, D., Lai, F., & Liu, S. (2022). Earth pressure in narrow cohesive-fictional soils behind retaining walls rotated about the top: An analytical approach. *Computers and Geotechnics*, *149*, Article 104849. https://doi.org/10.1016/j.compgeo.2022.104849

Computers and Geotechnics 149 (2022) 104849

Contents lists available at ScienceDirect

Computers and Geotechnics

journal homepage: www.elsevier.com/locate/compgeo

Earth pressure in narrow cohesive-fictional soils behind retaining walls rotated about the top: An analytical approach

Dayu Yang [a], Fengwen Lai [a,b,*], Songyu Liu [a]

[a] Institute of Geotechnical Engineering, Southeast University, Nanjing 211189, PR China
[b] Faculty of Civil Engineering and Geosciences, Delft University of Technology, Building 23, Stevinweg 1 / PO-box 5048, 2628 CN Delft / 2600 GA Delft, The Netherlands

ARTICLE INFO

Keywords:
Earth pressure
Narrow soil
Finite element limit analysis
Arched differential element method
Soil arching effect

ABSTRACT

There is currently a lack of an available design approach to estimate the earth pressure in narrow backfills behind retaining walls rotated about the top (RT). The considerations of some significant factors, primarily load transfer mechanisms (soil arching effect and horizontal shear stress in soils), failure mechanisms (shape and number of slip surfaces) and soil cohesion are often neglected for brevity in routine design. Such simplifications may lead to significant deviations from reality. This paper first uses the finite element limit analysis (FELA) technique to identify the underlying failure mechanisms and load transfer mechanisms. The results observed in FELA models indicate that active rotation of walls about the top develops one curved slip surface, which can be approximated by the log-spiral function. Under the soil arching effect, the upper intermediate passive zone with major principal stress rotation trajectory and the lower active zone with minor one can be defined. The arched differential element method (ADEM) is then introduced to formulate the earth pressure calculation. The results from newly published tests, existing analytical approaches, and FELA are compared to validate the accuracy of the proposed approach in both purely-frictional and cohesive-frictional soils. Parametric studies are further conducted to thoroughly understand the earth pressure problems, considering the effects of sensitive design variables (e.g. aspect ratio, soil strength parameters, and wall-soil interface friction angle). The analytical approach presented here would be a great extension to the design guidelines for the retaining structures with narrow backfills.

1. Introduction

Retaining structures unavoidably need to be constructed around existing structures (e.g. basement, pile groups, diaphragm walls) adjacent to an excavation, or rock faces to maintain the stability of backfills somewhere in between, forming narrow soils, as shown in Fig. 1 (Li and Yang, 2019; Chen et al., 2019; Xie et al., 2020; Chen et al., 2021 Lai et al., 2021; Lai et al., 2022a,b). The estimation of earth pressure exerted onto retaining walls is a traditional and still ongoing field of research, in particular under complex boundary conditions (Ni et al., 2018a; Ni et al., 2018b). Traditional Coulomb's or Rankine's theories (Coulomb, 1776; Rankine, 1857) for earth pressure calculation behind rigid retaining walls assumed that the rupture of retained soils took place along one single slip surface, forming a triangular failure body. This assumption was based upon sufficient width of soil mass, which thus may not be applicable to narrow soils where complex failure mechanisms characterized with trapezoid thrust wedge could occur. Moreover, for the anchored/strutted walls or bridge abutments where are embedded in the soft/weak soils and the movements at the top are partially limited, the rotation mode about the top (RT) is likely to be formed at the limit state (Fang and Ishibashi, 1986; Harrop-Williams, 1989; Ni et al., 2017; Deng and Haigh, 2020). This mode is inconsistent with the translational (T) one typically assumed by the traditional theories. The neglect of these factors might cause the given solution to deviate from the real one for retaining walls under RT mode (Terzaghi, 1936). For this reason, the search for improved analytical approaches to obtain a more accurate solution remains a key goal of many geotechnical researchers.

Previous experimental studies (Fang and Ishibashi, 1986; Frydman and Keissar, 1987; Take and Valsangkar, 2001) have reported that the distribution of active earth pressure against retaining structures with narrow soils is nonlinear along with the wall depth, resulting from the soil arching effect proposed by Terzaghi (1943). To obtain a more profound understanding of underlying load transfer mechanisms, many experimental works were further carried out over the last decade (O'Neal et al., 2011; Yang and Tang, 2017; Rui et al., 2020). However, due to the increasing complexity of simulated working conditions as

* Corresponding authors at: Institute of Geotechnical Engineering, Southeast University, Nanjing 211189, PR China.
E-mail addresses: yang_dayu@163.com (D. Yang), laifengwen@163.com, F.Lai-1@tudelft.nl (F. Lai), liusy@seu.edu.cn (S. Liu).

https://doi.org/10.1016/j.compgeo.2022.104849
Received 28 February 2022; Received in revised form 14 May 2022; Accepted 27 May 2022
Available online 15 June 2022

Nomenclature

$a_1 - a_4$	Abbreviations used in the derivation process
B	Width of narrow soils behind retaining wall (m)
$b_1 - b_5$	Abbreviations used in the derivation process
$C_1 - C_4$	Abbreviations used in the derivation process
c	Soil cohesion (kPa)
c_1, c_2	Abbreviations used in the derivation process
E_0	Young's modulus (MPa)
E_{total}	Thrust acting on rotating retaining wall (kN)
$F_x^{A_1D_1}$, $F_x^{A_1'D_1'}$	Horizontal forces on upper and lower boundaries of the element in upper zone (kN)
$F_z^{A_1D_1}$, $F_z^{A_1'D_1'}$	Vertical forces on upper and lower boundaries of the element in upper zone (kN)
$F_x^{A_1A_1'}$, $F_x^{D_1D_1'}$	Horizontal forces on wall-soil interface involved in the element in upper zone (kN)
$F_z^{A_1A_1'}$, $F_z^{D_1D_1'}$	Vertical forces on wall-soil interface involved in the element in upper zone (kN)
$F_x^{A_3D_3}$, $F_x^{A_3'D_3'}$	Horizontal forces on upper and lower boundaries of the element in lower zone II(kN)
$F_z^{A_3D_3}$, $F_z^{A_3'D_3'}$	Vertical forces on upper and lower boundaries of the element in lower zone II(kN)
$F_x^{A_3A_3'}$	Horizontal forces on wall-soil interface involved in the element in lower zone II (kN)
$F_z^{A_3A_3'}$	Horizontal forces on wall-soil interface involved in the element in lower zone II (kN)
$F_x^{D_3D_3'}$	Vertical forces on slip surface involved in the element in lower zone II (kN)
$F_z^{D_3D_3'}$	Vertical forces on slip surface involved in the element in lower zone II (kN)
G_1	Gravity of arched differential element in upper zone (kN)
G_2	Gravity of arched differential element in lower zone II (kN)
H	Retaining wall height (m)
H_1	Height of the upper zone (m)
H_2	Height of the lower zone I (m)
H_3	Height of the lower zone II (m)
K_0	Coefficient of lateral earth pressure at rest
K_{total}	Total thrust coefficient
$l_{A_3D_3}$	Length of A_3D_3 (m)
$l_{D_3D_3'}$	Curve length of D_3D_3' (m)
$m_1 - m_3, m_R, m_z$	Abbreviations used in derivation process
N	Ratio of major to minor principal stresses
$p_1 - p_{19}$	Optimal constant coefficients
$R_{A_1D_1}$	Radius of minor principal stress trajectory (m)
$R_{A_3D_3}$, $R_{A_3D_3'}$	Radius of major principal stress trajectory (m)
r_0	Initial polar radius of the log spiral (m)
$t_1 - t_3$	Abbreviations used in derivation process
$w_1 - w_3$	Abbreviations used in derivation process
z_s	Application point of active thrust to wall base (m)
$\triangle z_1$	Vertical distance between points A_1 and i (m)
$\triangle z_3$	Vertical distance between points A_3 and i (m)
α_f	Sliding angle of slip surface (°)
β	Correction factor of active thrust coefficient
θ_1	Angle of the log spiral at the wall toe
θ_2	Angle parameter of the log spiral equation at the stable wall
θ_w	Rotation angle of minor principal stress on wall-soil interface to the horizontal
θ_s	Rotation angle of minor principal stress on slip surface to the horizontal
γ	Unit weight (kPa)
ϕ	Soil friction angle (°)
δ	Wall-soil interface friction angle (°)
μ	Interface roughness factor
ν	Poisson's ratio
$\sigma_w^0, \sigma_w^u, \sigma_w^{l_1}, \sigma_w^{l_2}$	Lateral earth pressure exerted in upper and lower zones (kPa)
σ_1^0, σ_3^0	Major and minor principal stresses on wall-soil interface (kPa)
σ_f, τ_f	Normal and shear stresses on slip surface (kPa)
σ_1^i	Major principal stress at arbitrary point i on the upper boundary of the element (kPa)
σ_3^i	Minor principal stress at arbitrary point i on the upper boundary of the element (kPa)

well as the huge cost of resources, the development of experiments remains relatively slow. In addition, experimental efforts paid close attention to cohesionless soils (granular backfills), little to cohesive-frictional soils that are likely encountered in some cases (Yang and Yin, 2004; Yang and Huang, 2011; Li and Yang, 2019; Lai et al., 2022a).

To overcome the shortcomings mentioned above, many pieces of research were presented using cost-effective and powerful numerical tools such as finite element method (FEM) (Fang et al., 1993; Fan and Fang, 2010) and discrete element method (DEM) (Jiang et al., 2014). Recently, a novel numerical method of finite-element limit analysis (FELA), with the balance between accuracy and efficiency (Sloan, 2013), has been widely used in earth pressure problems (Chen et al., 2020; Krabbenhoft, 2018; Lai et al., 2022a). The current numerical works attempted to identify the failure mechanisms of the retaining system more realistically, under various movement modes including the translation (T), rotation about the base (RB), and the top (RT). Numerical results showed that irrespective of wall movement modes, most of the observed slip surfaces extending from the bottom of retaining walls are curved ones rather than planar ones, which have been also found in some experimental researches (Goel and Patra, 2008; Yang and Tang, 2017; Rui et al., 2020). In the theoretical aspect, the curved failure surface was generally described as the well-accepted log-spiral one (Xie and Leshchinsky, 2016; Xu et al. 2019; Chen et al., 2021).

Based on the experimental and numerical results, a series of analytical approaches have been proposed by many researchers. Among them, the horizontal differential element method (HDEM) is the most representative as the soil arching effect could be evaluated quantitatively by formulating the rotation trajectories of minor/major principal stresses. However, HDEM often neglects the horizontal shear stress between adjacent elements for brevity. Moreover, a necessary introduction of the lateral stress ratio requires defining the average vertical stress across a given differential element instead of the real vertical stress on the wall-soil interface, somehow causing the error. For this purpose, Lai et al. (2022a) proposed an improved analytical framework using the arched differential element method (ADEM) to overcome such disadvantages and to give more accurate solutions. Nevertheless, ADEM proposed by Lai et al. (2022a) is suggested to use for relatively simpler RB mode and might be incompatible with RT mode. The lack of analytical approach concerning the RT mode can be attributed as: (1) differing from the traditional Coulomb slip surface (planar), the log-spiral one involved in narrow backfills under the RT mode is difficult to mathematically characterize (Das and Sobhan, 2013); and (2) active wall rotation about the top would generate highly stressed zones in shallow layers, causing a counterintuitive phenomenon of shallowly

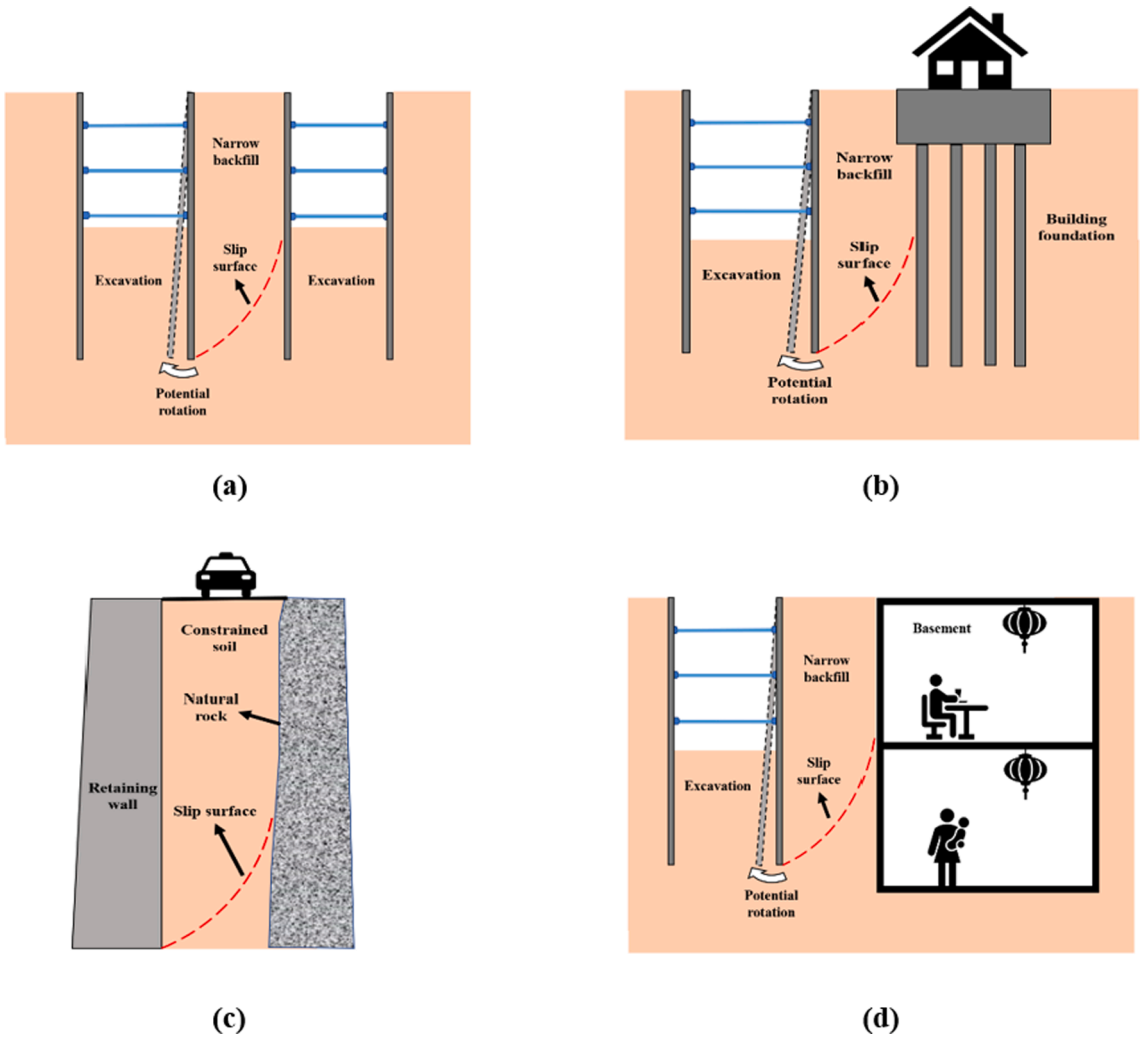

Fig. 1. Practical examples of retaining walls with narrow soils: (a) adjacent excavations; (b) excavation near pile foundations; (c) montane highway and; (d) excavation near basements.

embedded backfills entering the intermediate passive state (Deng and Haigh 2021). Our research group is thus expected to present an available analytical framework, allowing the underlying failure mechanisms and complex load transfer mechanisms of retaining structures under RT mode to be taken into account.

This study aims to present an analytical approach to estimate the earth pressure in narrow cohesive-frictional soils behind rotating walls about the top. In what follows, the failure mechanisms and load transfer mechanisms of narrow cohesive-frictional soils are first interpreted by FELA. On this basis, we establish a calculation model composed of upper and lower stress zones where the rotation trajectories of major and minor principal stresses are distinguished. The ADEM is subsequently employed to derive the mathematical expressions for calculating the earth pressure in narrow soils. The proposed solutions are validated against the previous experimental data, FELA results, and existing analytical solutions, both in cohesionless soils and cohesive soils. A parametric study is further conducted to understand the change laws of earth pressure and resulting thrust as well as the height of the application point.

2. Preliminary numerical work

FELA is an advanced numerical technique incorporating both the limit plastic theorem and the generalized variational principle. The exact solution (e.g. limit load or safety factor) can be bracketed between the upper bound (UB) and the lower bound (LB) solutions given by FELA. More details can be found in Sloan (2013).

In this paper, a commercial FELA software, Optum G2 (Academic edition), was chosen to study the earth pressure problems of narrow backfill behind the wall under the RT mode. The software is capable of automatically generating finite-element mesh using adaptive mesh refinement in light of a specific target (generally shear dissipation band). The FELA solutions are obtained by multi-iterations to quickly approximate the real solution. These advantages provide immense convenience for the investigation into complex failure mechanisms under various working conditions. Till now, Optum G2 has been extensively used to solve a variety of geotechnical problems (Ukritchon and Keawsawasvong, 2016; Khatri et al., 2017; Chen et al., 2019; Lai et al., 2020; Lai et al., 2022a).

2.1. Problem definition

The active responses of the retaining system under the RT mode are investigated by the problem definition presented in Fig. 2 (a). Cohesive-frictional soils with unit weight γ, cohesion c, and friction angle ϕ are assumed to be homogenous and isotropic. Two vertical rigid retaining walls with height (H) were placed on both sides of the backfill with a narrow width (B). The walls are considered rough and the wall-soil interface friction angle is δ. A roughness factor μ of $\tan\delta/\tan\phi$ can be thus defined to characterize the degree of interface roughness, and the

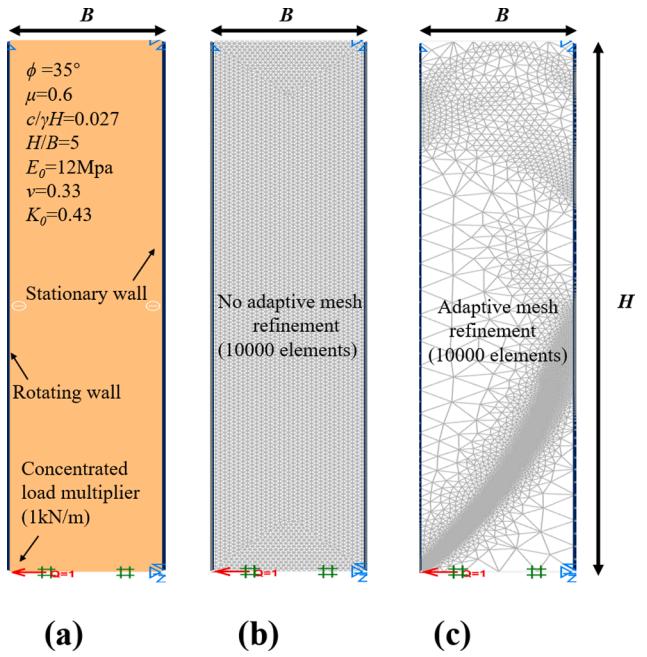

Fig. 2. FELA model under plane strain condition: (a) geometric configuration; (b) mesh generation without adaptive mesh refinement and (c) mesh generation with adaptive mesh refinement.

Table 1
Model parameters of cohesive-frictional soil adopted in FELA.

Soil parameter	Value	Reference
Unit weight [γ (kN/m3)]	18.5	Deduced from Lai et al. (2022a)
Cohesion [c (kPa)]	5	
Friction angle [ϕ (∘)]	25	
Friction angle of wall-soil interface [δ (∘)]	15.63	
Young's modulus [E_0 (MPa)]	12	
Poisson's ratio (ν)	0.33	
Coefficient of lateral earth pressure at rest (K_0)	0.43	

interface adhesion is $\mu \cdot c$. A summarization of basic model parameters is shown in Table 1.

2.2. Numerical model details

In the established numerical model, the top boundary was set to be free while the bottom boundary was perfectly constrained. The right-side wall was then fully fixed; but for the left-side wall, rotation at the top was permitted while the horizontal and vertical displacements were constrained. A horizontal concentrated load multiplier of 1kN/m was thus imposed on the toe of the left-side wall to produce the active RT failure mode.

In the process of meshing, 6-node Gauss elements were generated in the soil domain as well as retaining walls were modeled by weightless rigid plate elements, where soil-structure elements were also automatically created along with the depth at the wall-soil interface. The soils followed an elastic, perfectly plastic Mohr-Coulomb (MC) model where the associated flow rule was selected under drained conditions. It is significant to be noted that although the associated flow rule, inherently employed in FELA, is somewhat unrealistic in practice, it provides clearer shear bands than non-associated flow rule (Tschuchnigg et al., 2015), which is of course beneficial for the observation of the underlying failure mechanisms. The influences of flow rule on the estimation of earth pressure are worthy of further numerical investigations as the analytical approach presented following does not address this issue. It is, however, clearly out of the scope of the paper. In addition, to capture the potential shear bands, the initially generated mesh would be refined according to the energy of shear dissipation, and the number of mesh gradually increased from 5, 000 to 10, 000 during the iteration [Fig. 2 (b-c)].

2.3. Failure mechanisms

During the numerical simulation, four dimensionless parameters, including aspect ratio (H/B), normalized soil cohesion ($c/\gamma H$), soil friction angle(ϕ), and roughness factor (μ) of the wall-soil interface were set as control variables.

Fig. 3 illustrates the influence of the variables in turn (i.e., H/B, $c/\gamma H$, ϕ, μ). As shown in Fig. 3a, for narrow soils, a curved failure surface develops from the rotating wall toe and then interacts with the stable wall. The height of the failure surface observed remains unchanged when increasing aspect ratio (backfill height). It also means that if reducing backfill width at a fixed backfill height, the initial rupture angles (sliding angles) to the horizontal (α_f) theoretically are almost the same, as reported by Lai et al. (2022a). It is without a doubt that the larger soil cohesion is beneficial for keeping the stability of retaining systems, however, the soil cohesion seems to have a smaller effect on the shape of the failure surface (Fig. 3b). From Fig. 3c, we can see that both the total height of the failure surface and initial rupture angle α_f increase obviously with the increase of soil friction angle. Fig. 3d indicates that an increase of the roughness factor of the wall-soil interface leads to the reduction in the initial rupture angle α_f, but the height of the slip surface's height behaves oppositely.

In all, it can be concluded from the observed failure mechanism that the narrow soils behind retaining walls undergoing RT mode only have one curved slip surface, and the variation of initial rupture α_f is mainly governed by frictional behaviors of soils and wall-soil interfaces. This provides an important basis for the establishment of the following calculation model.

2.4. Arching-induced principal stress rotation

The phenomenon of principal stress rotation is typically introduced to quantitatively characterize the soil arching effect of retaining structures, therein the mathematical description of the rotation trajectory shape of major and minor principal stresses (σ_1 and σ_3) is essential for the use of HDEM or ADEM. While for the active rotation/translation of retaining walls, the soil arching effect is generally characterized by mathematically describing the rotation trajectory of σ_3. It follows that the bow-shaped distribution of earth pressure along with the wall depth would be seen (Paik and Salgado, 2003; Chen et al., 2019; Lai et al., 2022a). That is, the point of maximum active earth pressure is located around the wall toe. However, this intuitionistic phenomenon does not well match with the experimental results under the RT mode reported by Deng and Haigh (2020) and Xu et al. (2022). Using centrifuge tests, Deng and Haigh (2020) pointed out that the shallow layer of backfills forms a highly-stressed zone, causing the earth pressure at the top to increase with the active wall movements. This is because the wall movement mode of RT restricts the displacement of shallowly-embedded soils, but promotes the collapse of deeply-embedded soils.

To thoroughly explain this intuitionistic phenomenon, the principal stress rotation induced by the soil arching effect is illustrated in Fig. 4b. Compared to Lai et al. (2022a), the upper zone in the figure appears the continuous rotation trajectories of σ_1, rather than those of σ_3. Therefore, we believe that the so-called "highly-stressed zone" at the top can be explained by mechanisms of active trapdoor problems (e.g. tunneling and piping). In addition, the lower zone sketched in the figure is like the assemblage of upper and lower zones described by Lai et al. (2022a), although the shapes of failure surfaces are various (see Fig. 4a).

It follows from Fig. 4b that the depth of transition between the upper and the lower zones almost corresponds to the embedded depth of the

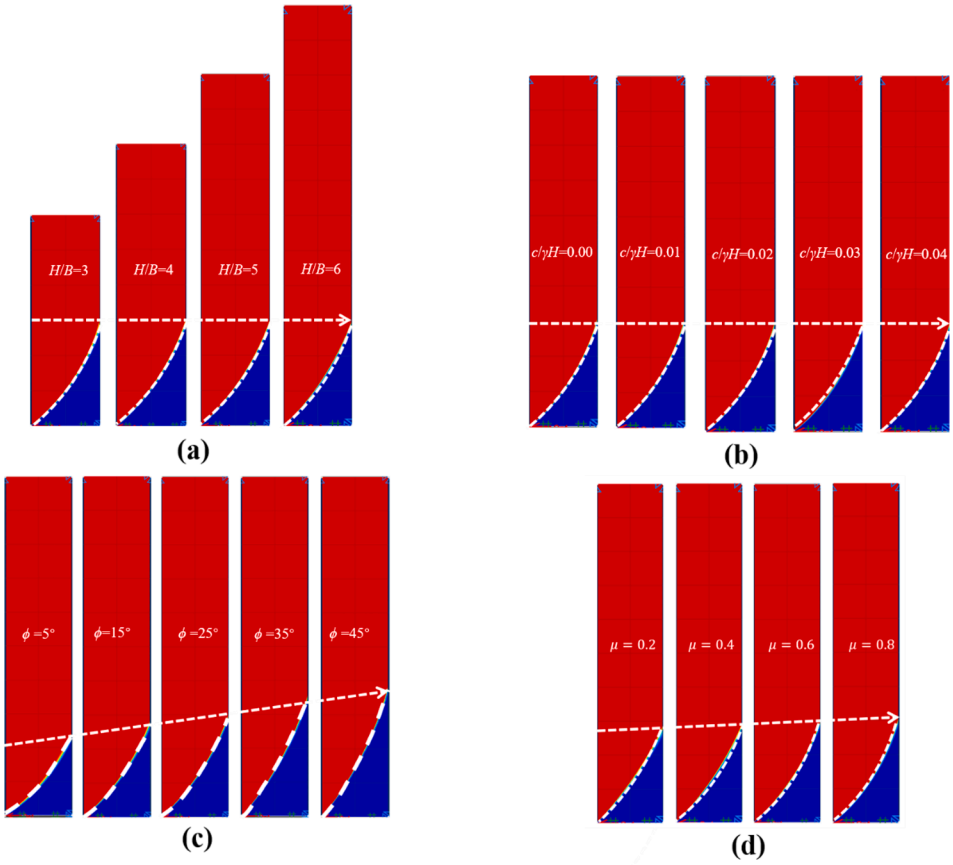

Fig. 3. Effect of four dimensionless parameters on the failure mode of narrow soils behind rotating wall about the top: (a) aspect ratio ($c/\gamma H = 0.027$, $\phi = 25°$ and $\mu = 0.6$); (b) soil cohesion ($H/B = 0.2$, $c/\gamma H = 0.027$ and $\mu = 0.6$); (c) soil friction angle ($H/B = 0.2$, $c/\gamma H = 0.027$ and $\phi = 25°$) and (d) roughness factor ($H/B = 0.2$, $\phi = 35\circ$ and $\mu = 0.6$).

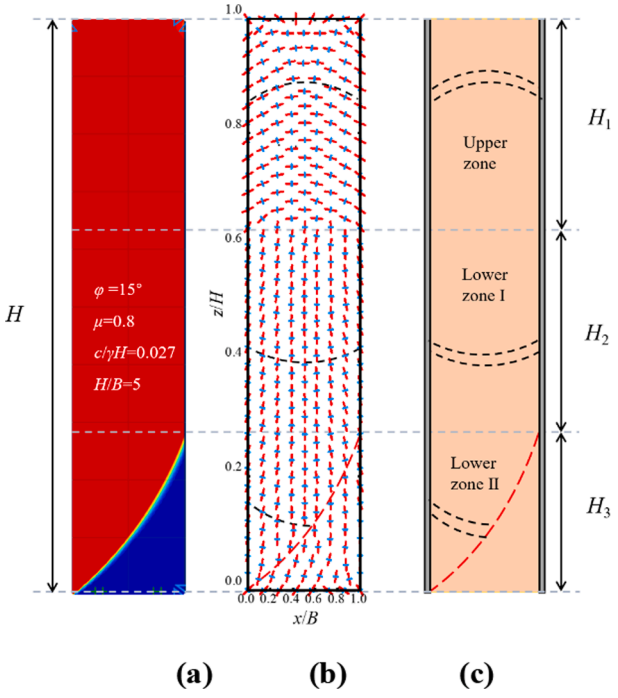

Fig. 4. FELA observations: (a) failure mode; (b) rotation of principal stresses and (c) established calculation model.

Table 2
Optimal value of constant coefficients for closed-form approximation.

Optimal parameter	Value
p_1	−1.363
p_2	1.351
p_3	12.486
p_4	0.017
p_5	3.581
p_6	0.466
p_7	0.383

trapdoor. It means that the height of upper zone may correspond to the critical soil arch height of determined with high complexity. It was reported that the critical soil arch height is mainly determined by trapdoor width and soil friction angle, and the soil cohesion has a negligible effect (Low et al., 1994; Horgan and Sarsby, 2002; Naughton and Kempton, 2005; Lu and Miao, 2015;). For retaining structures, the wall-soil interface friction factor should be of course involved for the soil arching problem. To confirm our inference, the heights of the upper zone (H_1) in various cases obtained using FELA are summarized in Table A1 of Appendix A. The table clearly show the effect of soil cohesion on the height of the upper zone can be almost neglected, hence supporting the reasonability of the above inference. Due to a fact that the value of H_1 is difficult to mechanically determine using analytical approach. Alternatively, a best-fitted equation with a coefficient of determination (R^2) of 94.56%, based on the FELA results in Table A1, is presented to approximately calculate the height of the upper zone:

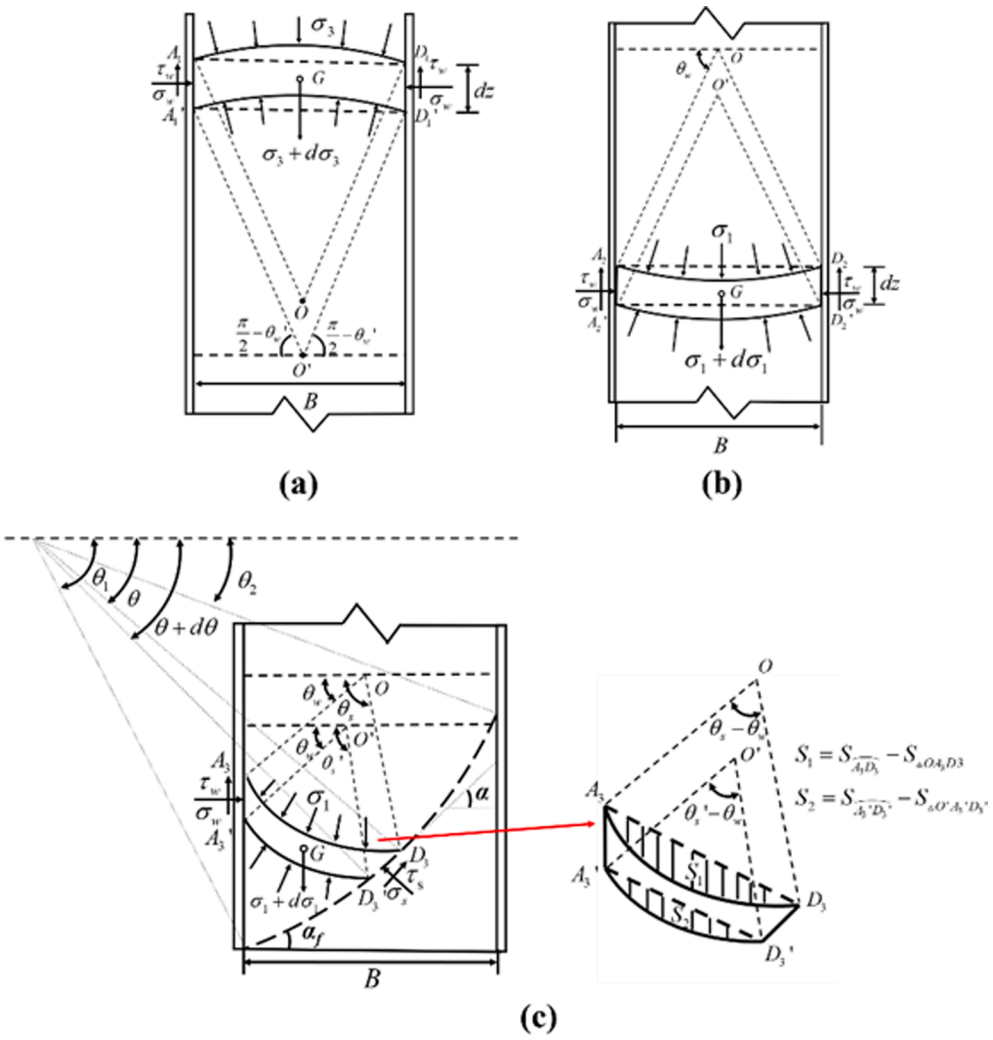

Fig. 5. Calculation model in: (a) upper zone; (b) lower zone I and (c) lower zone II.

$$H_1 = [\frac{(B/H)^{p_1}(p_4 + p_5\tan\delta + p_6\tan\phi)}{1 + p_2\tan\varphi + p_3\tan\delta} - (p_7 - \tan\delta)^2]B \quad (1)$$

where p_1-p_7 are constant coefficients tabulated in Table 2.

The shape of rotation trajectories of principal stresses also attracted the attention of many researchers. They attempted to use elliptic, catenary, parabolic, or circular-arc-shaped curves to formulate rotation trajectories of principal stresses. Lai et al. (2022a) have demonstrated that the rotation trajectories of σ_3 well follow the circular-arc function, as also seen in Fig. 4 (b). In fact, among them, the circular-arc trajectory is well-accepted and recommended in some literature (Handy, 1985; Paik and Salgado, 2003; Chen et al., 2017; Cao et al., 2020; Lai et al., 2022a), as it can be more easily described using mathematical equations. Here we still select the circular-arc to approximate the rotation trajectories of σ_1 or σ_3.

3. Calculation framework

3.1. Basic assumptions

To formulate the earth pressure in narrow backfills under the RT mode, a calculation model is established considering both load transfer mechanisms and failure mechanisms, as shown in Fig. 4c. Some basic assumptions are made for simplification, as follows:

(1) The active rotation of retaining walls about the top is sufficient to cause the active limit state of soil and full mobilization of wall-soil interface strength.

(2) The slip surface developed from the wall toe follows a log-spiral curve with an initial rupture angle α_f between the slip surface and the horizontal obtained using Coulomb's theory, as below:

$$\alpha_f = \arctan(\sqrt{\tan^2\phi + \frac{\tan\phi}{\tan(\phi+\delta)}} + \tan\phi) \quad (2)$$

(3) The rotation trajectories of both major principal stress in the upper zone and minor principal stress in the lower zone are assumed to be circular arcs.

3.2. Derivation procedure

3.2.1. Upper zone

The formulations for earth pressure exerted into narrow cohesive-frictional soils in the upper zone under the RT mode are derived in this part. According to the interpreted load transfer mechanisms, arched differential element $A_1A_1'D_1'D_1$ with a thickness of dz [Fig. 5 (a)] is constructed along the rotation trajectories of major principal stresses.

Considering FELA observations in Fig. 4 (b) and 5 (a), the rotation angle θ_w is given as.

$$\theta_w = \arctan(\frac{N - 1 - \sqrt{(N-1)^2 - 4N\tan^2\delta}}{2\tan\delta}) \quad (3)$$

where N is the coefficient obtained by the MC failure criterion, and

can be written as.

$$N = \frac{\sigma_1 + c\cot\phi}{\sigma_3 + c\cot\phi} = \tan^2(\frac{\phi}{2} + \frac{\pi}{4}) \tag{4}$$

The more detailed derivations of θ_w can be found in Appendix B.

The rotation trajectory of σ_1 is considered to be the circular-arc, as shown in Fig. 5 (a), the radius $R_{A_1D_1}$ of the circular arc thus calculated using.

$$R_{A_1D_1} = \frac{B}{2\sin\theta_w} \tag{5}$$

It is assumed that the minor principal stress on the boundary A_1D_1 linearly increases with the height difference Δz_1 between point A_1 and the arbitrary point i. Namely,

$$\sigma_3^i = \sigma_3^0 + \gamma\triangle z_1 \tag{6}$$

where σ_3^0 is the minor principal stress at point A_1 and σ_3^i is the minor principal stress at arbitrary point i.

From Fig. 5 (a), we can see.

$$\triangle z_1 = R_{A_1D_1}(\sin\theta_w - \sin\theta) \tag{7}$$

There are only minor principal stresses acting on A_1D_1. The vertical resulting force $F_z^{A_1D_1}$ on A_1D_1 can be thus calculated:

$$F_z^{A_1D_1} = 2\int_{\frac{\pi}{2}-\theta_w}^{\frac{\pi}{2}} \sigma_3^i R_{A_1D_1}\sin\theta d\theta \tag{8}$$

Substituting Eqs. (6) and (7) into Eq. (8) leads to.

$$F_z^{A_1D_1} = 2\sigma_3^0 R_{A_1D_1}\sin\theta_w - \gamma R_{A_1D_1}^2(\frac{\theta_w}{2} + \frac{\sin2\theta_w}{4} - \sin^2\theta_w) \tag{9}$$

Similarly, vertical resulting force on $A_1'D_1'$ can be obtained:

$$F_z^{A_1'D_1'} = 2(\sigma_3^0 + d\sigma_3^0)R_{A_1D_1}\sin\theta_w - \gamma R_{A_1D_1}^2(\frac{\theta_w}{2} + \frac{\sin2\theta_w}{4} - \sin^2\theta_w) \tag{10}$$

The vertical resulting forces on lateral boundaries, A_1A_1' and D_1D_1', are calculated using.

$$F_z^{A_1A_1'} = F_z^{D_1D_1'} = (\sigma_w + c\cot\phi)\tan\delta dz = (\sigma_1^0 + c\cot\phi)(\cos^2\theta_w + \frac{\sin^2\theta_w}{N})\tan\delta dz \tag{11}$$

Moreover, the gravity of arched differential element $A_1A_1'D_1'D_1$ is.

$$G_1 = \gamma B dz \tag{12}$$

Now we can establish the vertical mechanical equilibrium equation, as follows:

$$F_z^{A_1A_1'} + F_z^{D_1D_1'} + F_z^{A_1'D_1'} - F_z^{A_1D_1} = G_1 \tag{13}$$

Substitution of Eqs. (9), (10), (11) and (12) into Eq. (13) yields.

$$\frac{d\sigma_3^0}{dz} + C_1\sigma_3^0 + C_2 = 0 \tag{14}$$

where.

$$C_1 = \frac{N(\cos^2\theta_w + \frac{\sin^2\theta_w}{N})\tan\delta}{R\sin\theta_w} \tag{15}$$

$$C_2 = -\frac{\gamma B - 2c\cot\phi\tan\delta}{2R\sin\theta_w} \tag{16}$$

Solving Eq. (14) gives.

$$\sigma_3^0 = \frac{C_2}{C_1}(e^{-C_1 z} - 1) \tag{17}$$

Further substituting Eq. (4), Eq. (B. 1) into Eq. (17), the earth pressure of narrow cohesive-frictional soils in the upper zone can be obtained as.

$$\sigma_w^u = N(\sigma_3^0 + c\cot\phi)(\cos^2\theta_w + \frac{\sin^2\theta_w}{N}) - c\cot\phi \tag{18}$$

3.2.2. Lower zone

The determination of the earth pressure in the lower zone can be divided into two parts, according to the force condition. The first part is that both sides of the rotation trajectory of minor principal stress (the element $A_2A_2'D_2'D_2$ in Fig. 5b) are wall-soil interfaces. Differently, the second part is that one side is the wall-soil interface and the other side is the curvilinear slip surface. It is thus necessary to calculate the total height of two parts, and then calculate their earth pressure, respectively.

As described above, the equation of the log-spiral slip surface is given as.

$$r(\theta) = r_0 e^{\theta\tan\varphi} \tag{19}$$

where $r(\theta)$ is the polar radius of the log spiral, θ is the angle of any points on the slip surface within the polar coordinate system, and r_0 is the initial polar radius of the log spiral, which can be expressed as.

$$r_0 = \frac{B}{e^{\theta_2\tan\phi}\cos\theta_2 - e^{\theta_1\tan\phi}\cos\theta_1} \tag{20}$$

where θ_1 is the angle of the log spiral at the wall toe, θ_2 is the angle parameter of the log spiral equation at the stable wall. The derivations of r_0, θ_1 and θ_2 can be found in Appendix C.

Thus, the height H_3 of the lower zone II can be expressed as.

$$H_3 = r_0(e^{\theta_1\tan\phi}\sin\theta_1 - e^{\theta_2\tan\phi}\sin\theta_2) \tag{21}$$

The height H_2 of the lower zone I can be further given as.

$$H_2 = H - H_1 - H_3 \tag{22}$$

The force derivation in lower zone I (Fig. 5b) is like that of the upper zone mentioned by Lai et al. (2022a). Therefore, a detailed derivation can refer to Lai et al. (2022a). Note that, the magnitude of the major principal stress on the rotating wall between the upper and the lower zones should be continuous, which is adopted as the boundary condition for solutions. Here we can give the expression of earth pressure in lower zone I, as described by.

$$\sigma_w^{l_1} = (\cos^2\theta_w + \frac{\sin^2\theta_w}{N})[\frac{C_4}{C_3}(e^{-C_3 z} - 1) + Q + c\cot\varphi)] - c\cot\varphi \tag{23}$$

where.

$$C_3 = \frac{(\cos^2\theta_w + \frac{\sin^2\theta_w}{N})\tan\delta}{R\cos\theta_w} \tag{24}$$

$$C_4 = -\frac{\gamma B - 2c\cot\phi\tan\delta}{2R\cos\theta_w} \tag{25}$$

$$Q = -\frac{C_4}{C_3}(e^{-C_3 H_1} - 1) + \frac{C_2}{C_1}(e^{-C_1 H_1} - 1) \tag{26}$$

The rotation angle θ_s of major principal stress on slip surface to the horizontal can be given as.

$$\theta_s = \frac{\pi}{4} - \frac{\phi}{2} + \alpha = \frac{3\pi}{4} + \frac{\phi}{2} - \theta \tag{27}$$

The derivation of θ_s is showed in Appendix A.

According to the geometric relationships in Fig. 5 (c), we have.

$$\angle A_3OD_3 = \theta_s - \theta_w \tag{28}$$

$$\angle OA_3A_3' = \theta_w + \frac{\pi}{2} \tag{29}$$

Combining Eqs. (28) and (29) gives.

$$\angle D_3A_3A_3' = \frac{\theta_w + \theta_s}{2} \tag{30}$$

Further according to the geometric relationships in Fig. 5 (c), we obtain.

$$l_{A_3D_3} = \frac{r(\theta)\cos\theta - r(\theta_1)\cos\theta_1}{\sin(\frac{\theta_w+\theta_s}{2})} \tag{31}$$

The radius of $R_{A_3D_3}$ can be thus provided as.

$$R_{A_3D_3} = \frac{l_{A_3D_3}}{\sin(\frac{\angle A_3OD_3}{2})} \tag{32}$$

Substituting Eqs. (28) and (31) into Eq. (32) to get.

$$R_{A_3D_3} = \frac{r(\theta)\cos\theta - r(\theta_1)\cos\theta_1}{2\sin(\frac{\theta_w+\theta_s}{2})\sin(\frac{\theta_s-\theta_w}{2})} \tag{33}$$

Similarly, the radius of σ_3 rotation trajectory on the lower boundary and the accompanied arc length in the element $A_3A_3'D_3'D_3$ can be expressed as

$$R_{A_3'D_3'} = \frac{r(\theta+d\theta)\cos(\theta+d\theta) - r(\theta_1)\cos\theta_1}{2\sin(\frac{\theta_w+\theta_s'}{2})\sin(\frac{\theta_s'-\theta_w}{2})} \tag{34}$$

The major principal stress on the boundary A_3D_3 is assumed to linearly increase with the height difference Δz_3 between point A_3 and arbitrary point i (Lai et al., 2022a), which can be expressed as

$$\sigma_1^i = \sigma_1^0 + \gamma\triangle z_3 \tag{35}$$

where σ_1^0 is the major principal stress at point A_3 and σ_1^i is the major principal stress at arbitrary point i. And Δz_3 can be expressed as

$$\triangle z_3 = R_{A_3D_3}(\sin\theta_w - \sin\theta) \tag{36}$$

The horizontal and vertical forces on the upper boundary of arched differential element $A_3A_3'D_3'D_3$ can be thus determined by the integration, as follows:

$$F_x^{A_3D_3} = \int_{\theta_w}^{\theta_s} \sigma_1^i R_{A_3D_3}\cos\theta d\theta = \sigma_1^0 R_{A_3D_3}t_1 + \frac{1}{2}\gamma R_{A_3D_3}^2 t_1^2 \tag{37}$$

$$F_z^{A_3D_3} = \int_{\theta_w}^{\theta_s} \sigma_1^i R_{A_3D_3}\sin\theta d\theta = \sigma_1^0 R_{A_3D_3}t_2 + \gamma R_{A_3D_3}^2 t_3 \tag{38}$$

where.

$$t_1 = \sin\theta_s - \sin\theta_w \tag{39}$$

$$t_2 = \cos\theta_w - \cos\theta_s \tag{40}$$

$$t_3 = \frac{\theta_s-\theta_w}{2} - \frac{\sin2\theta_s + \sin2\theta_w}{4} + \cos\theta_s\sin\theta_w \tag{41}$$

Similarly, the horizontal and vertical forces on the lower bound of differential element $A_3A_3'D_3'D_3$ thus can be expressed as.

$$F_x^{A_3'D_3'} = (\sigma_1^0 + d\sigma_1^0)(m_1R_{A_3D_3} + m_Rt_1) + \frac{1}{2}\gamma(t_1^2R_{A_3D_3}^2 + 2m_RR_{A_3D_3}t_1^2 + 2m_1t_1R_{A_3D_3}^2) \tag{42}$$

$$F_z^{A_3'D_3'} = (\sigma_1^0 + d\sigma_1^0)(m_2R_{A_3D_3} + m_Rt_2) + \gamma(t_3R_{A_3D_3}^2 + 2m_Rt_3R_{A_3D_3} + m_3R_{A_3D_3}^2) \tag{43}$$

where

$$m_1 = -\cos\theta_s \tag{44}$$

$$m_2 = -\sin\theta_s \tag{45}$$

$$m_3 = -\frac{1}{2} + \frac{\cos(2\theta_s)}{2} + \sin\theta_s\sin\theta_w \tag{46}$$

$$m_R = \frac{dR_{A_3D_3}(\theta)}{d\theta} \tag{47}$$

Considering $x_{D_3} - x_{A_3} = r(\theta)\cos\theta - r(\theta_1)\cos\theta_1$, the ordinate $z(\theta)$ of A_3 can be expressed as

$$z(\theta) = r(\theta)\sin\theta - \frac{r(\theta)\cos\theta - r(\theta_1)\cos\theta_1}{\tan(\frac{\theta_w+\theta_s}{2})} - r(\theta_1)\sin\theta_1 + H \tag{48}$$

Moreover, the length dz of the boundary A_3A_3' can be given as

$$dz = m_z d\theta \tag{49}$$

where

$$m_z = \frac{\partial z(\theta)}{\partial\theta} \tag{50}$$

The horizontal and vertical forces acting on boundaries A_3A_3' and D_3D_3' can be provided as

$$F_x^{D_3D_3'} = l_{D_3D_3'}(-\sigma_f sin\alpha + \tau_f cos\alpha) \tag{51}$$

$$F_z^{D_3D_3'} = l_{D_3D_3'}(\sigma_f\cos\alpha + \tau_f\sin\alpha) \tag{52}$$

$$F_x^{A_3A_3'} = (\sigma_w^0 + c\cot\phi)dz = (\sigma_1^0 + c\cot\phi)(\cos^2\theta_w + \frac{\sin^2\theta_w}{N})dz \tag{53}$$

$$F_z^{A_3A_3'} = (\sigma_w^0 + c\cot\phi)\tan\delta dz = (\sigma_1^0 + c\cot\phi)(\cos^2\theta_w + \frac{\sin^2\theta_w}{N})\tan\delta dz \tag{54}$$

where σ_f is the normal stress on the slip surface, τ_f is the shear stress on the slip surface.

The curve length $l_{D_3D_3'}$ can be calculated, as follow:

$$l_{D_3D_3'} = \sqrt{r^2(\theta) + r'(\theta)^2}d\theta \tag{55}$$

The weight of the arched differential element $A_3A_3'D_3'D_3$ in Fig. 5 (c) can be calculated as.

$$G_2 = \gamma(S_{A_3A_3'D_3'D_3} - S_1 + S_2) \tag{56}$$

where

$$S_1 = S_{A_3D_3} - S_{\Delta OA_3D_3} = R_{A_3D_3}^2[\theta_s - \theta_w - \frac{\sin(\theta_s-\theta_w)}{2}] \tag{57}$$

$$S_2 = S_{A_3'D_3'} - S_{\Delta O'A_3'D_3'} = (R_{A_3D_3}^2 + 2m_RR_{A_3D_3}d\theta)[\theta_s' - \theta_w - \frac{\sin(\theta_s'-\theta_w)}{2}] \tag{58}$$

$$S_{AA'D'D} = \frac{(l_{A_3D_3} + l_{A_3'D_3'})m_z\sin\angle DAA'}{2}d\theta = m_z[r(\theta)\cos\theta - r(\theta_1)\cos\theta_1]d\theta \tag{59}$$

Substituting Eqs. (57), (58) and (59) into Eq. (56), we obtain.

$$G_2 = \gamma\{m_z[r(\theta)\cos\theta - r(\theta_1)\cos\theta_1] + R_{A_3D_3}^2[\cos(\theta_s-\theta_w) - 1] + 2m_RR_{A_3D_3}[\theta_s - \theta_w - \sin(\theta_s-\theta_w)]\}d\theta \tag{60}$$

The mechanical components involved in the horizontal and vertical mechanical equilibrium equations can be written as:

$$F_x^{A_3A_3'} - F_x^{A_3D_3} + F_x^{A_3'D_3'} + F_x^{D_3D_3'} = 0 \tag{61}$$

$$F_z^{A_3A_3'} - F_z^{A_3D_3} + F_z^{A_3'D_3'} + F_z^{D_3D_3'} - G_2 = 0 \tag{62}$$

Substituting the corresponding variables into Eqs. (61) and (62), we have

$$(a_1 + a_4)\sigma_1^0 d\theta + a_2 d\sigma_1^0 + a_3 d\theta + l_{D_3D_3'}c_1\sigma_f = 0 \tag{63}$$

$$(b_1 + b_4)\sigma_1^0 d\theta + b_2 d\sigma_1^0 + (b_3 - b_5)d\theta + l_{D_3D_3'}c_2\sigma_f = 0 \tag{64}$$

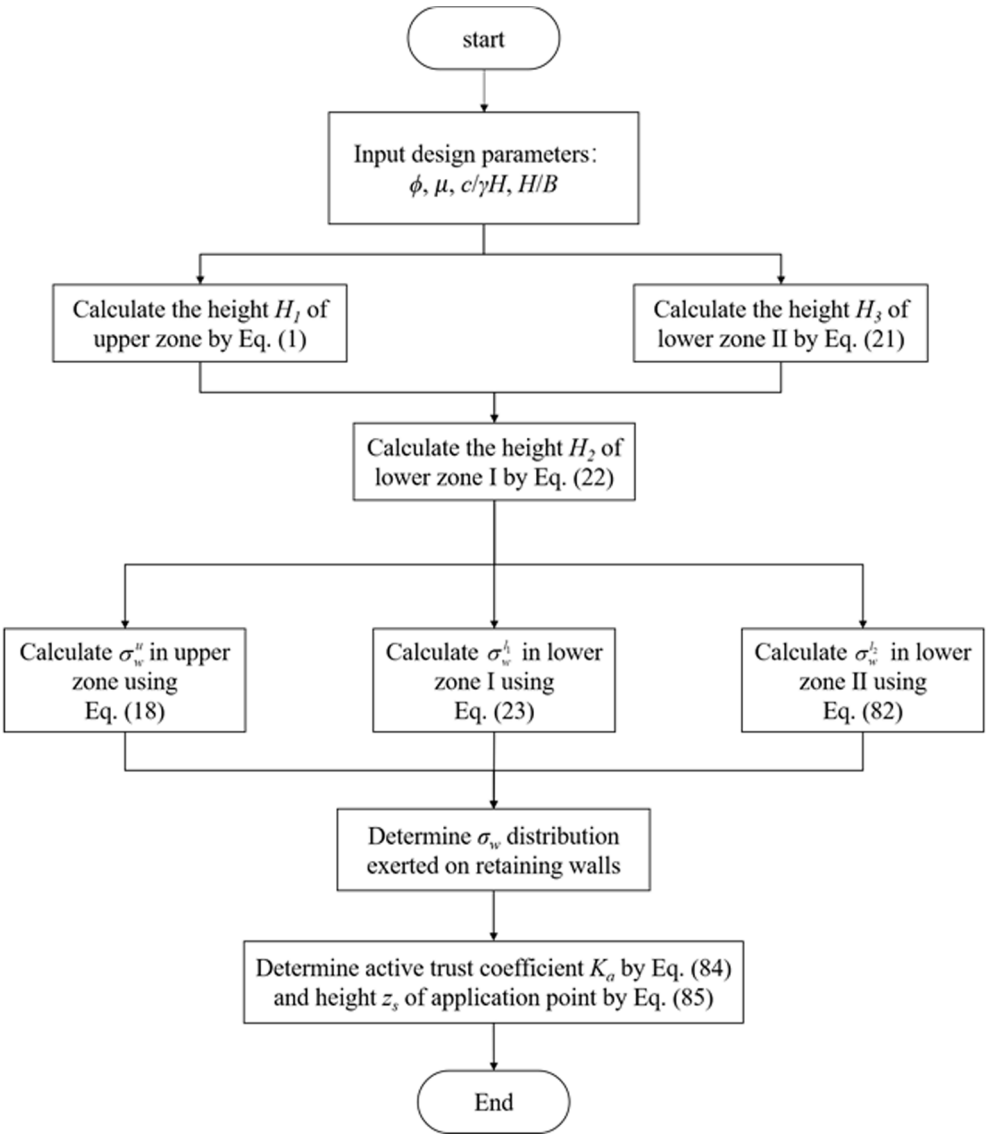

Fig. 6. Calculation flowchart.

where

$$a_1 = m_1 R_{A_3D_3} + m_R t_1 \tag{65}$$

$$a_2 = t_1 R_{A_3D_3} \tag{66}$$

$$a_3 = \gamma(t_1 R_{A_3D_3}^2 m_1 + m_R t_1^2 R_{A_3D_3}) + c\cot\phi(\cos^2\theta_w + \frac{1}{N}\sin^2\theta_w) + \sqrt{r^2(\theta) + r'(\theta)^2}\, c\cos\alpha \tag{67}$$

$$a_4 = m_z(\cos^2\theta_w + \frac{1}{N}\sin^2\theta_w) \tag{68}$$

$$b_1 = m_2 R_{A_3D_3} + m_R t_2 \tag{69}$$

$$b_2 = t_2 R_{A_3D_3} \tag{70}$$

$$b_3 = \gamma(m_3 R_{A_3D_3}^2 + 2m_R R_{A_3D_3} t_3) + c\tan\delta\cot\phi(\cos^2\theta_w + \frac{1}{N}\sin^2\theta_w) + \sqrt{r^2(\theta) + r'(\theta)^2}\, c\sin\alpha \tag{71}$$

$$b_4 = m_z\tan\delta(\cos^2\theta_w + \frac{1}{N}\sin^2\theta_w) \tag{72}$$

$$b_5 = \gamma\{m_z[r(\theta)\cos\theta - r(\theta_1)\cos\theta_1] + R_{A_3D_3}^2[\cos(\theta_s - \theta_w) - 1] + 2m_R R_{A_3D_3}[\theta_s - \theta_w - \sin(\theta_s - \theta_w)]\} \tag{73}$$

$$c_1 = \tan\phi\cos\alpha - \sin\alpha \tag{74}$$

$$c_2 = \cos\alpha + \tan\phi\sin\alpha \tag{75}$$

Substituting Eq. (63) into Eq. (64) to eliminate σ_f provides.

$$w_1\sigma_1^0 d\theta + w_2 d\sigma_1^0 + w_3 d\theta = 0 \tag{76}$$

Thus,

$$\frac{d\sigma_1^0}{d\theta} + \frac{w_1}{w_2}\sigma_1^0 + w_3 = 0 \tag{77}$$

where

$$w_1 = (a_1 + a_4)c_2 - (b_1 + b_4)c_1 \tag{78}$$

$$w_2 = a_2 c_2 - b_2 c_1 \tag{79}$$

$$w_3 = a_3 c_2 - (b_3 - b_5)c_1 \tag{80}$$

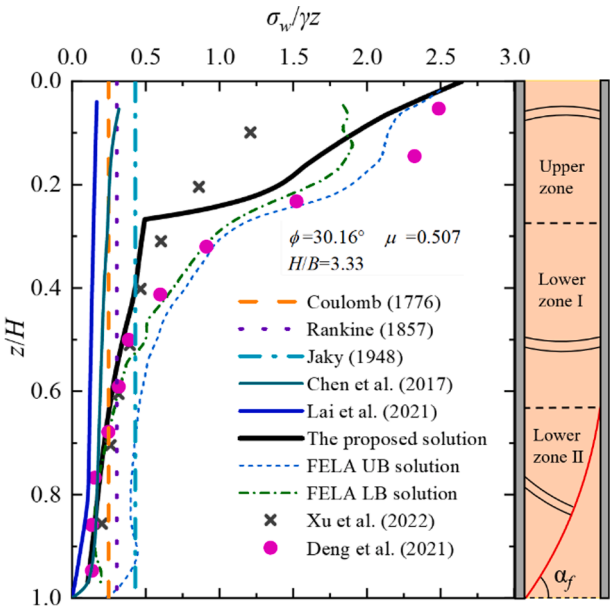

Fig. 7. Comparisons among the results from the proposed approach, model experiment, centrifuge test FELA, and existing theoretical solutions for cohesionless soils.

We can solve Eq. (77), which is a first-order differential equation for the major principle stress, using a finite-difference method, as written by:

$$\sigma_1^0(\theta+\Delta\theta)=\sigma_1^0(\theta)-\frac{w_1\sigma_1^0+w_3}{w_2}\Delta\theta \tag{81}$$

Then, according to Eq. (4), the earth pressure in narrow cohesive-frictional soils of the lower zone II can be expressed as

$$\sigma_w^{l_2}=(\cos^2\theta_w+\frac{\sin^2\theta_w}{N})(\sigma_1^0+c\cot\phi)-c\cot\phi \tag{82}$$

3.3. Total thrust and height of application point

To meet the requirements in engineering design, and to provide engineers with more intuitive parameters to evaluate the retaining wall ability against overturning, equations for calculating total thrust of narrow soil and the corresponding height of application point based on the proposed method are given, as below:

$$E_{total}=\int_0^{H_1}\sigma_w^u dz+\int_{H_1}^{H_1+H_2}\sigma_w^{l_1}dz+\int_{H_1+H_2}^{H}\sigma_w^{l_2}dz \tag{83}$$

Eq. (83) can be expressed in the dimensionless form:

$$K_{total}=\frac{2E_{total}}{\gamma H^2} \tag{84}$$

where K_{total} is defined as the thrust coefficient based on Coulomb's earth pressure theory.

Further calculating the moment on the wall toe, the height z_s of the application point of earth thrust to the wall toe can be consequently obtained:

$$z_s=\frac{\int_0^{H_1}\sigma_w^u(H-z)dz+\int_{H_1}^{H_1+H_2}\sigma_w^{l_1}(H-z)dz+\int_{H_1+H_2}^{H}\sigma_w^{l_2}(H-z)dz}{E_{total}} \tag{85}$$

3.4. Calculation flowchart

A calculation flowchart is given in Fig. 6, showing key steps to obtain the distribution of earth pressure along the wall depth, and key design parameters (i.e. K_{total} and z_s/H) for a routine design. An in-house Python code (see supplementary material) is employed for running the calculation. At the first step, four dimensionless variables, i.e., H/B, $c/\gamma H$, ϕ, and μ will be required to input in the program. Then, the height of the three stress zones will be determined. The subsequent calculation will be processed following the proposed analytical approach, which involves comprehensive considerations of the soil arching effect and the induced stress rotation, the shearing force between adjacent elements, the soil cohesion, as well as curved (log-spiral) slip surfaces.

4. Comparisons and validations

As emphasized by Lai et al. (2022a), to take an analytical approach into a routine geotechnical problem (e.g. retaining wall design), it should be comprehensively assessed using well-established and relatively-controllable laboratory tests or numerical simulation. Moreover, comparing traditional theories and existing analytical approaches are an effective means for showing the strengths of a newly presented approach. Here, the lateral earth pressure in both narrow cohesionless and cohesive soils obtained from the proposed approach will be compared with the data from model tests, FELA, and existing analytical approaches.

4.1. Cohesionless soils

The model tests exploring the earth pressure distribution of narrow cohesionless soil behind retaining walls under RT mode were conducted by Xu et.al (2022) and were introduced here as a benchmark to validate the proposed analytical approach. In model tests, a rigid wall was constructed to retain narrow backfills with a height of 1 m and a width of 0.3 m, hence $H/B=3.3$. Fujian standard sand was selected as backfilled material with a friction angle of 30.16° and a unit weight of 14.5 kN/m^3. The roughness factor of the wall-soil interface was 0.507. More detailed parameters can refer to Xu et al. (2022). On this basis, we produce a FELA numerical model to obtain the upper bound (UB) and lower bound (LB) solutions. The results from traditional theories [e.g. Jaky's, Rankine's, and Coulomb's solutions] and two existing analytical approaches for narrow backfills under the T (Chen et al., 2017) and RT modes (Lai et al., 2022a) are further used for the comparison, respectively.

Fig. 7 presents the comparisons among the proposed approach, model tests, FELA solutions, traditional theories, and existing analytical approaches. It can be found that, compared with the current theoretical solutions, the proposed approach provides the best approximation to the measured values from Xu et al. (2022) and FELA solutions. A slight deviation from the measured values in the upper zone might be due to the scale effect of model tests. The accuracy of the proposed approach can be thus confirmed.

Interestingly, we observe that both the measured values of normalized earth pressure coefficient $\sigma_w/\gamma z$ and the proposed solutions in the upper zone are much larger than the solutions given by traditional theories based on the backfills with semi-infinite space at rest or the active state. Further comparisons with two existing analytical approaches aiming at T and RB modes are no exception. From observations and comparisons, the proposed solutions in the upper zone are closer to Rankine's passive solutions, however, the earth pressures in the lower zone are mobilized towards an active state. As emphasized earlier, this counterintuitive phenomenon can be explained using the experimental work by Deng and Haigh (2020). This also confirms soils in the upper zone form a highly-stressed zone which enters the intermediate passive state with active wall rotation. The introduction of σ_1 rotation trajectory in the proposed analytical approach more accurately quantifies the soil arching effect in the upper zone, differing from that in the existing analytical approaches (σ_3 rotation trajectory). The two existing analytical approaches under the T and the RB modes are confirmed to be unsafe for the practical design of retaining walls undergoing the RT mode. Therefore, we recommend using the proposed analytical approach to estimate the earth pressure exerted by narrow soils behind active

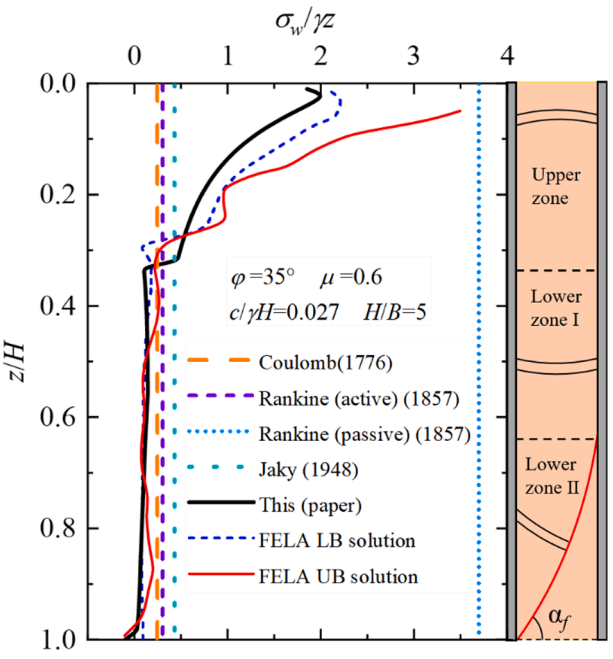

Fig. 8. Comparisons among the results from the proposed approach, FELA, and traditional theories for cohesive-frictional soils.

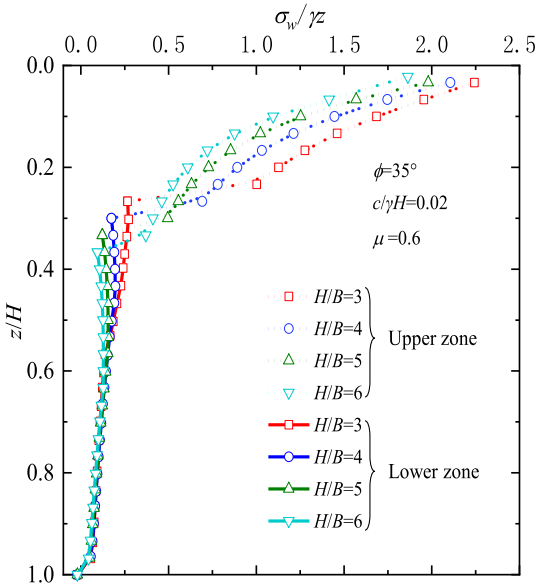

Fig. 9. Normalized active earth pressure distribution along wall depth with varying aspect ratio.

rotating walls about the top.

4.2. Cohesive-frictional soils

Till now, to the best of the author's knowledge, experimental studies of earth pressure's distribution are mainly focused on cohesionless soils, few on cohesive-frictional soils. Therefore, a FELA model is established here for validation. The inputted model parameters refer to Lai et al. (2022a). The UB and LB solutions of FELA are obtained and then compared in Fig. 8. The traditional theories are also introduced for comparisons. The figure shows that the proposed approach can perfectly fit numerical results for cohesive soils. It can be found that compared with traditional solutions, the solutions proposed in this paper have

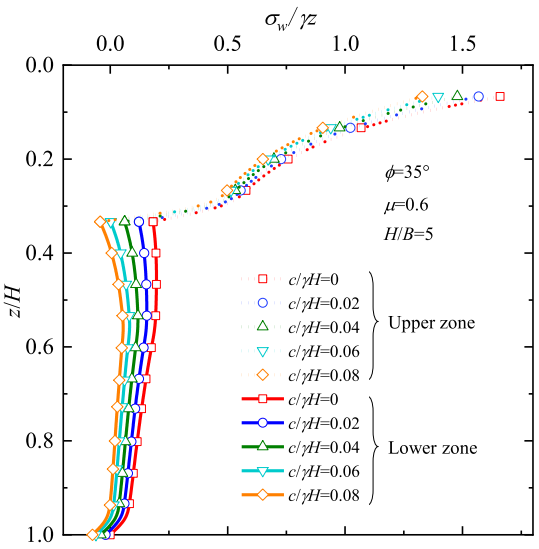

Fig. 10. Normalized active earth pressure distribution along wall depth with varying cohesion.

higher accuracy in describing the nonlinear distribution of earth pressure of narrow backfills under the RT mode. Traditional solutions deviate greatly from real ones, which further illustrates the importance of this approach. The active state of the lower zone and the intermediate passive state of the upper zone are also clearly seen in Fig. 8.

5. Parametric study

A parametric study of the proposed analytical approach was carried out in this section. Sensitive influencing parameters, including aspect ratio (H/B), normalized soil cohesion ($c/\gamma H$) and soil friction angle (ϕ), wall-soil interface roughness factor (μ), were selected for parameter analyses. Normalized earth pressure coefficient $\sigma_w/\gamma z$, thrust coefficient K_{total} and height of application point of active thrust to the base z_s/H, generally regarded as routine indicators for retaining wall design, were calculated under various working conditions. It should be noted that the objective of a parametric study is to better guide the engineering design. Therefore, the calculated parameters should cover the practical ranges. For this purpose, the aspect ratio is set from 3 to 6, the normalized soil cohesion ($c/\gamma H$) is varied from 0 to 0.08, the soil friction angle covers from 5° to 45°, and the wall-soil interface roughness factor was in a range of 0.2 to 0.8 (Lai et al. 2022a).

5.1. Effect of aspect ratio

The effect of aspect ratio on the distribution of the earth pressure $\sigma_w/\gamma z$ along the normalized depth z/H is plotted in Fig. 9. Due to the division of various stress zones, the earth pressure in the upper zone is obviously higher than that in the lower zone. It also follows that the earth pressure $\sigma_w/\gamma z$ at a given z/H decreases with an increase of H/B for both the upper zone and the lower zone. This is due to the increase of H/B, the ratio of the contact friction at the wall-soil interface to the gravity of narrow soils increases, leading to a more remarkable soil arching effect. Therefore, the consideration of a narrower backfill width can yield a more economic design scheme. The obvious variation in $\sigma_w/\gamma z$ with the aspect ratio greatly confirms the necessity of presenting a design method to estimate the earth pressure exerted by narrow backfill.

In essence, the height of the upper zone will have a significant impact on the distribution of earth pressure as the upper and lower zones have various stress states (intermediate passive and active). In light of Eq. (1), the height of the upper zone increases with an increase of the aspect ratio H/B, as seen in Fig. 9. It is of significance to understand the

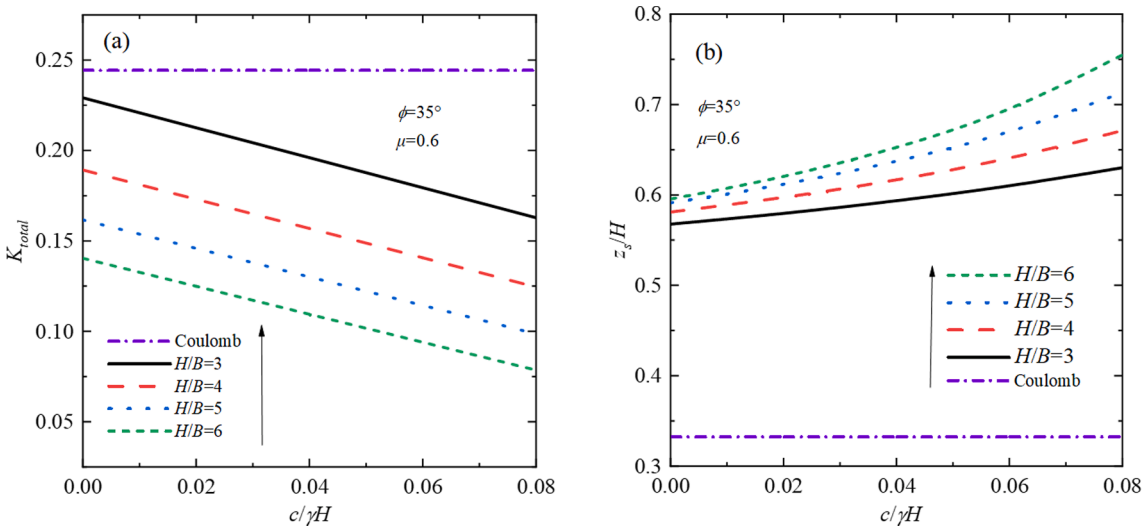

Fig. 11. Effect of normalized soil cohesion under various aspect ratios on: (a) thrust coefficient and (b) normalized height of application point of thrust to wall base.

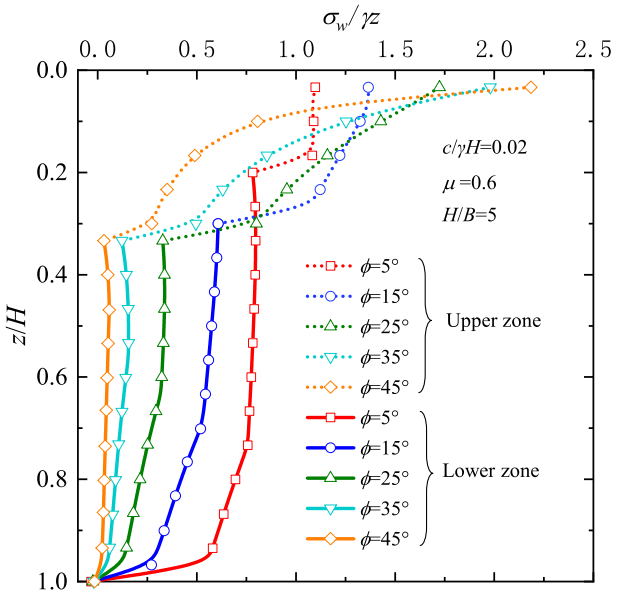

Fig. 12. Normalized earth pressure distribution along wall depth with varying soil friction angle.

formation mechanism of the upper zone. Deng and Haigh (2020) pointed out that the active wall rotation about the top constrains the displacement of the shallowly-buried soil, but promotes the collapse of the deeply-buried soil. On this basis, decreasing backfill width at a given backfill height (equivalently increasing the H/B ratio), intensifies the constraint of narrow backfills, in particular for the upper zone.

5.2. Effect of soil cohesion

Although clean, coarse-grained, well-drained granular materials (e.g. gravels) are typically used as backfill materials, cohesive soils are sometimes used as backfill materials for an economic purpose (Li and Yang 2019; Lai et al. 2022a). Anderson (2008) reported that the earth pressure in cohesive soils with the cohesion of 10kpa is significantly lowered to 25–50% of that in cohesionless soils, the neglection of soil cohesion likely results in an enormous overestimation of earth pressure. To improve the solution in cohesive soils, this part attempts to explore the influence of cohesion on the earth pressure problem of narrow backfill under the RT mode.

Fig. 10 presents the variation in earth pressure $\sigma_w/\gamma z$ along wall depth z/h for various soil cohesion. As shown in Fig. 10, $\sigma_w/\gamma z$ decreases when increasing the soil cohesion for a fixed wall depth. Despite the soil cohesion varies, the distribution law of $\sigma_w/\gamma z$ remains unchanged. The reason can be given as: (i) The soil cohesion has a negligible influence on the shape of slip surface, the rotation trajectory of principal stress, and the division of calculation zones. (ii) The proposed analytical approach, based on the elastic-perfectly plastic Mohr-Coulomb failure criteria, neglects the effect of tensile loading (Lai et al. 2022a).

The effect of soil cohesion on the thrust coefficient K_{total} and the height of application point to the base z_s/H are further plotted in Fig. 11 (a) and 11 (b). It can be observed from Fig. 11(a) that increasing soil cohesion produces a linear reduction in K_{total}. Correspondingly, the reduction magnitude of K_{total} can be up to approximately 26%~42% as $c/\gamma H$ increases from 0 to 0.04, which supports the viewpoint of Anderson (2008). In Fig. 11 (b), completely differing from the RB mode (nonlinear decrease of z_s/H) studied by Lai et al. (2022a), the z_s/H increases in the shape of an inverted parabola as soil cohesion increases under the RT mode. This is because the reduction rate of resulting earth pressure by soil cohesion in the upper zone is always lower than that in the lower zone, essentially depending on the various stress states in the upper and lower zones. Therefore, the obtained z_s/H is also always larger than 1/3 suggested by Comlomb's theory. That is, the stability of rotating walls about the top is underestimated in Coulomb's theory. In conclusion, the considerations of calculation zone division and soil cohesion promote more accurate solutions. It should be pointed out that for clays with a higher effective cohesion, full mobilization of soil cohesion is not recommended to be used in practical design due to the strain-softening effect. A resulting residual soil cohesion is more reasonable on the safe side.

5.3. Effect of soil friction angle

Fig. 12 gives the distribution of $\sigma_w/\gamma z$ along z/H for various soil friction angles ϕ. It can be found that an increase of ϕ results in a notable increment of $\sigma_w/\gamma z$ in the upper zone and a corresponding reduction in the lower zone, respectively. This phenomenon can be explained by a fact that the higher the soil friction angle, the stronger the soil arching effect. The height of the upper zone increases with increasing ϕ to transfer more vertical loading by the arching, resulting in the larger earth pressure exerted onto the upper wall (see Fig. 12). In light of the two-stages-arching theorem proposed by Handy (1985), under a fixed vertical loading, the more loads the upper zone transfers, the less the

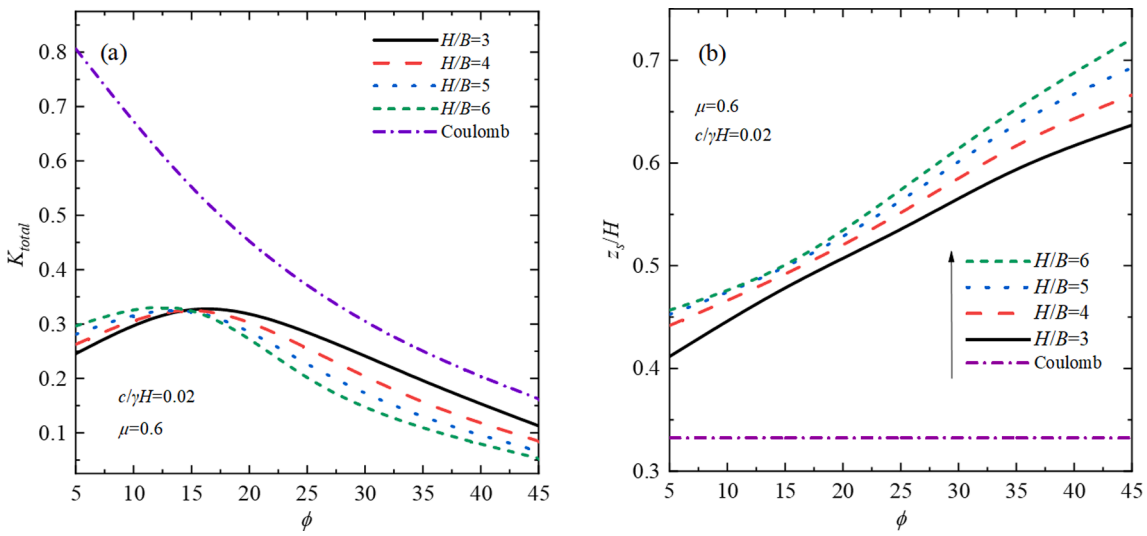

Fig. 13. Effect of soil friction angle under various aspect ratios on: (a) thrust coefficient and (b) normalized height of application point of thrust to wall base.

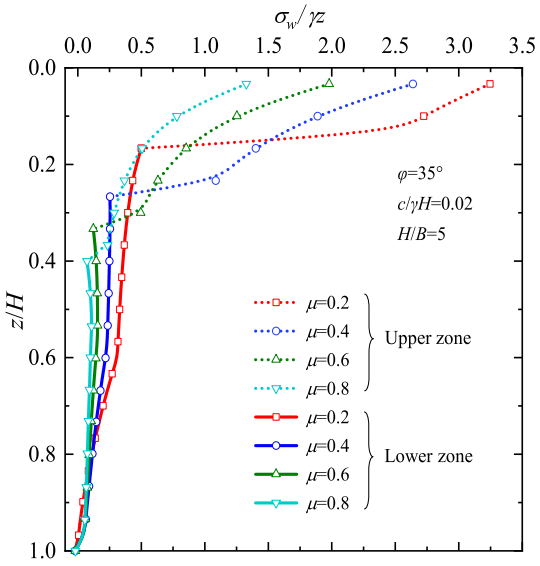

Fig. 14. Normalized active earth pressure distribution along wall depth with varying wall-soil interface roughness factor.

earth pressure exerted by the lower zone. In nature, it is consistent with the variations of passive and active earth pressure coefficients. When $\phi = 5°$, the values of $\sigma_w/\gamma z$ in both the upper and lower zones are close to 1.0, corresponding to a hydrostatic pressure coefficient, which demonstrates the accuracy of the proposed analytical approach in illustrating the influence of ϕ on the earth pressure problem.

The variations in K_{total} and z_s/H with ϕ under various H/B are plotted in Fig. 13 (a) and Fig. 13 (b), respectively. Differing from T (Chen et al., 2017) and RB modes (Lai et al., 2022a), the changing law of K_{total} with ϕ under RT mode is not monotonic, which is related to the discrepancy in the rotation trajectories of principal stress for various wall movement modes. Fig. 13 (a) shows that the resulting earth pressure (normalized thrust coefficient) first increases to a threshold, then decreases with an increase in ϕ. Accordingly, highly frictional materials are recommended here to use as backfills. It follows from Fig. 13 (b) that, the application point of the thrust moves up as ϕ increases due to the underlying load transfer mechanisms, indicating that the higher ϕ yields the better stability of retaining structures under RT mode. The account of strain-softening effect also should be taken into the choice of the backfilling materials in practice. Dense sands with a higher friction angle tend to be softening as the shear strains increase. For the short-term analyses, the strain-softening effect mainly occurs on the slip surface, especially near the wall toe, which leads to an increase in the earth pressure in the lower zone II. For the long-term one, the whole backfill domain may undergo the strain-softening, thus the residual ϕ is suggested to be employed towards a conservative design.

5.4. Effect of wall-soil interface roughness factor

The interface friction force of retaining structures is an essential factor to mobilize the soil arching effect, hence having a significant influence on the distribution of the earth pressure. A roughness factor $\mu = \tan\delta/\tan\phi$, known as the reduction coefficient of wall-soil interface strength, is introduced here for a quantitative evaluation of the effect of wall-soil interface friction angle δ. It should be noted that the soil friction angle ϕ is set as 35°, therefore, we only require varying angle δ.

Fig. 14 illustrates the distribution of $\sigma_w/\gamma H$ along z/H for various roughness factors μ. As shown in Fig. 14, as μ increases, the height of the upper zone increases and a reduction in $\sigma_w/\gamma H$ can be found in both upper and lower zones, meaning that increasing μ strengthens the soil arching effect. On the one hand, the increase of μ intensifies the restriction on the displacement of shallow soils, which facilitates the soils to approach the passive state. On the other hand, from the two-stages-arching theorem (Handy, 1985), the friction force provided from wall-soil interfaces transfers more gravity of backfills, hence reducing the earth pressure in both upper and lower zones for a given lateral earth pressure coefficient.

Fig. 15 (a) and 15 (b) plot the variations in K_{total} and z_s/H with μ under various H/B, respectively. As illustrated in Fig. 15 (a), for H/B varying from 3 to 5, K_{total} first increases to a threshold and then decreases with an increase of μ. However, when $H/B = 6$, K_{total} decreases with increasing μ. Such a strange phenomenon is due to the comprehensive effects of wall-soil interface friction and the variation of the upper zone. That is, although the more gravity is resisted by the interface for the larger μ, the height of the upper intermediate passive zone (the larger earth pressure exerted) increases according to Eq. (1). It again follows from Fig. 14, regardless of the change in heights of various zones, increasing angle δ will reduce the magnitude of $\sigma_w/\gamma H$ and has a more significant influence on the upper zone. Accordingly, in Fig. 15(b), we can observe a reduction in z_s/H with an increase of μ. We can infer from Fig. 15 (a) and 15(b) that the retaining structures with smooth interfaces and/or lower H/B tend to be more stable, and a comprehensive assessment into K_{total} and z_s/H is suggested to be made for μ greater

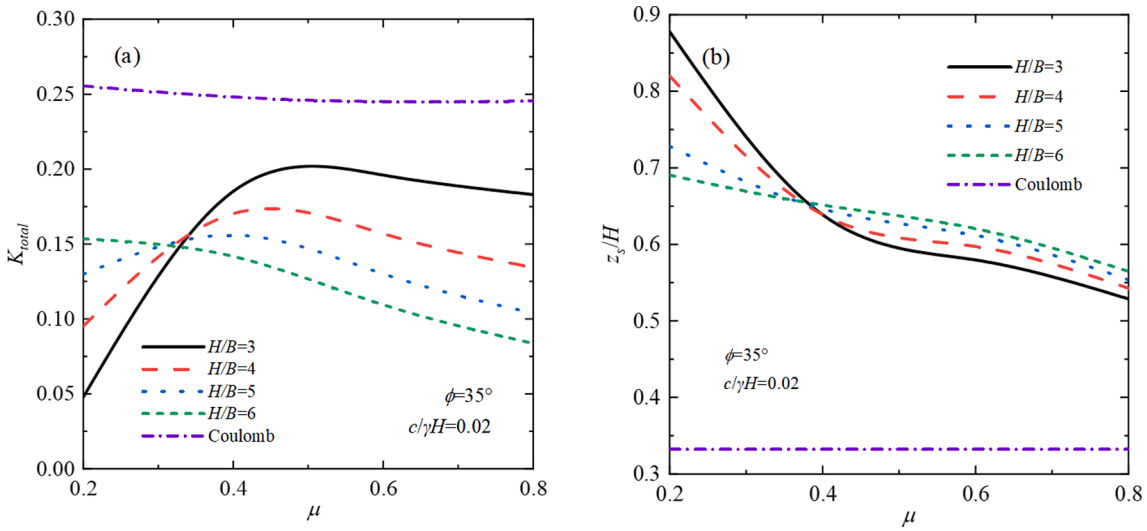

Fig. 15. Effect of wall-soil interface roughness factor under various aspect ratios on: (a) active thrust coefficient and (b) normalized height of application point of active thrust to wall base.

Table A1
Normalized height (H_1/B) of the upper zone obtained from Optum G2.

H/B	ϕ (°)	$\mu = 0.2$		$\mu = 0.4$		$\mu = 0.6$		$\mu = 0.8$		$\mu = 1.0$	
		$c/\gamma H = 0$	$c/\gamma H = 0.08$	$c/\gamma H = 0$	$c/\gamma H = 0.08$	$c/\gamma H = 0$	$c/\gamma H = 0.08$	$c/\gamma H = 0$	$c/\gamma H = 0.08$	$c/\gamma H = 0$	$c/\gamma H = 0.08$
3	5	0.10	0.10	0.20	0.20	0.40	0.40	0.50	0.50	0.50	0.50
	15	0.25	0.25	0.50	0.50	0.60	0.60	0.75	0.75	0.90	0.90
	25	0.20	0.20	0.50	0.50	0.70	0.70	0.70	0.70	1.25	1.25
	35	0.20	0.20	0.60	0.60	0.80	0.80	1.10	1.10	1.20	1.20
	45	0.25	0.25	0.50	0.50	0.60	0.60	1.20	1.20	1.10	1.10
4	5	0.15	0.15	0.50	0.50	0.60	0.60	0.75	0.75	0.90	0.90
	15	0.50	0.50	0.75	0.75	1.10	1.10	1.25	1.25	1.40	1.40
	25	0.50	0.50	0.75	0.75	1.10	1.10	2.00	2.00	1.65	1.65
	35	0.50	0.50	0.75	0.75	0.90	0.90	1.40	1.40	1.75	1.75
	45	0.50	0.50	0.77	0.77	1.00	1.00	1.50	1.50	1.50	1.50
5	5	0.20	0.20	0.70	0.70	0.90	0.90	1.10	1.10	1.25	1.25
	15	0.75	0.75	1.10	1.10	1.50	1.50	1.75	1.75	2.10	2.10
	25	0.75	0.75	1.20	1.20	1.70	1.70	2.00	2.00	2.25	2.25
	35	0.75	0.75	1.10	1.10	1.60	1.60	2.00	2.00	2.25	2.25
	45	0.50	0.50	1.00	1.00	1.50	1.50	1.90	1.90	2.00	2.00
6	5	0.55	0.55	0.90	0.90	1.20	1.20	1.50	1.50	1.75	1.75
	15	0.80	0.80	1.50	1.50	2.00	2.00	2.40	2.40	2.70	2.70
	25	1.00	1.00	1.50	1.50	2.20	2.20	2.60	2.60	3.00	3.00
	35	1.00	1.00	1.70	1.70	2.10	2.10	2.50	2.50	3.00	3.00
	45	0.80	0.80	1.25	1.25	1.90	1.90	2.20	2.20	2.50	2.50

than 0.4.

6. Limitations

The results have confirmed that the developed arched differential element method considering the intermediate passive zone well predicted the earth pressures of the narrow backfills under RT mode. There are, however, still somewhat imperfect due to a gap between practical conditions and the assumptions made. On the one hand, the consideration of the intermediate passive zone better characterizes the stress condition of shallow soils, resulting in the more reliable earth pressure distribution. On the other hand, due to the complexity involved, the determination of the height of the upper zone still relies on an empirical equation, which should be deduced based on a sound mechanical principal in the future.

Simplifying the rotation trajectory of principal stresses in backfill zone has some influences on the calculated results. It was postulated in this paper that the wall-soil interface strength is fully mobilized to derive the rotation angle of the principal stress on the wall-soil interface. However, for an actively rotating wall, the strength of the wall-soil interface is likely being only partially mobilized in practice. That is, the mobilization of the soil arching effect relevant to the frictional behavior of wall-soil interface may be somewhat overestimated in the proposed approach. As indicated in Fig. 7 and Fig. 8, too optimistic estimation of the mobilization of the wall-soil interface strength leads to a lower value of earth pressure under the soil arching effect. Additionally, the neglect of transition zone between the upper zone with rotation trajectory of σ_1 and lower zone with one of σ_3 results in a rapid jumping of earth pressure curve nearby. From the FELA results, there exhibits a gradually changing process in the rotation angles of principle stresses in the so-called transition zone. Towards a more precise estimation, more efforts are required to quantify the change laws of rotation angles of the principal stresses more accurately, in particular for the transition zones.

7. Conclusions

An improved arch differential element method, proposed by Lai et al. (2022a), comprehensively considering the effect of shear stress between

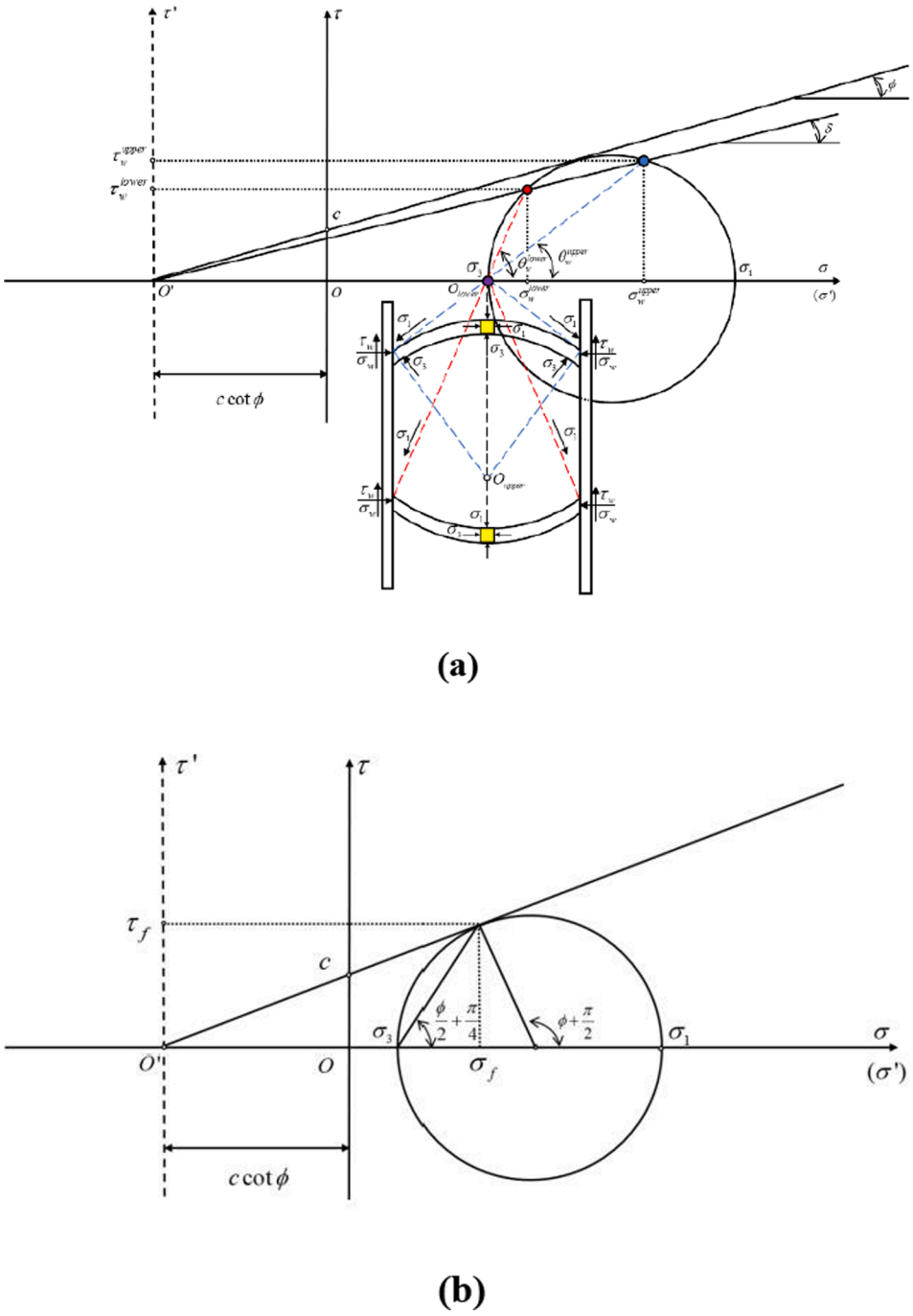

Fig. B1. Mohr circles of stresses at: (a) the wall and (b) the slip surface.

adjacent horizontal elements and the soil arching effect (rotation of principal stress), was successfully extended, and employed to estimate the earth pressure exerted by narrow backfills behind retaining structures under the RT mode. Before that, the failure mechanisms of the retaining system were interpreted by a novel FELA technique. Based on FELA results, two stress zones, including the upper and the lower zones, were divided in light of the rotation trajectories of principal stresses. Moreover, to search for a more accurate solution, the traditional (planar) Coulomb slip surface was replaced by a more realistic log-spiral slip surface, and the effect of soil cohesion was also considered for cohesive-frictional backfills for an economic purpose.

In-house python codes were then executed to obtain solutions to the proposed analytical approach. The comparisons among the results from recently published tests, FELA, existing analytical approaches, traditional theories, and the proposed solutions were carried out for validation. To understand the earth pressure problem in-depth, several key parameters (e.g. H/B, $c/\gamma H$, ϕ, and μ) were selected for parametric studies to investigate the associated effects on $\sigma_w/\gamma z$, K and z_s/H.

Based on the aforementioned analyses, the following conclusions can be drawn:

(1) The active rotation about the top of walls with narrow backfills develops only one curved slip surface, which is mathematically closer to be the log-spiral instead of a traditional Coulomb surface (planar). As the wall rotates, the backfills' stress redistributes, the upper intermediate passive zone with major principal stress rotation and lower active zone with minor one can be observed under the soil arching effect. Herein, the height of the upper zone

correlates positively with H/B, ϕ, and μ; but $c/\gamma H$ has a neglectful influence on it.

(2) For narrow cohesive-frictional backfills under the RT mode, the earth pressure in the upper zone is obviously higher than that in the lower zone in a specific case. Decreasing H/B and μ, and/or increasing $c/\gamma H$ can produce a reduction in the earth pressure in both the upper and the lower zones at a given depth. An increase of ϕ results in a notable increment of $\sigma_w/\gamma z$ in the upper zone, nevertheless a reduction in the lower zone.

(3) Under the drained condition, for a given H/B, highly frictional and/or cohesive materials are recommended to use as backfills because they are beneficial for reducing the earth thrust. The H/B and μ have a comprehensive effect on the thrust, showing that for $H/B = 3 \sim 5$, K first increases to a threshold and then decreases with an increase of μ. However, when $H/B = 6$, K decreases with increasing μ.

(4) The obtained z_s/H under the RT mode is always larger than 1/3 suggested by Comlomb's theory which underestimates the stability of rotating walls about the top. For a fixed H/B, the larger $c/\gamma H$ and ϕ, as well as the lower μ will move up the height of the application point, which is beneficial for maintaining the stability of retaining structures with narrow backfills.

CRediT authorship contribution statement

Dayu Yang: Methodology, Data curation, Writing – original draft. **Fengwen Lai:** Conceptualization, Writing – original draft, Writing – review & editing, Visualization, Software, Formal analysis. **Songyu Liu:** Supervision, Funding acquisition.

Declaration of Competing Interest

The authors declare that they have no known competing financial interests or personal relationships that could have appeared to influence the work reported in this paper.

Acknowledgements

This study is supported by the National Natural Science Foundation of China (Grant No. 41972269), Fundamental Research Funds for the Central Universities of China (Grant No. 2242022k30055), Postgraduate Research & Practice Innovation Program of Jiangsu Province (Grant No. KYCX20_0118) and Scientific Research Foundation of Graduate School of Southeast University (Grant No. YBPY2041).

Appendix A. . Numerical estimation of height of upper zone

100 groups of normalized heights (H_1/B) of upper zone in narrow backfills changing the aspect ratio ($H/B = 3$, 4, 5 and 6), soil friction angle ($\phi = 5$, 15, 25, 35 and 45°) and wall-soil interface roughness factor ($\mu = 0.2$, 0.4, 0.6, 0.8 and 1.0) are obtained using FELA. The results are illustrated in Table A1.

Appendix B. . Derivation of the rotation angle of principal stress

Fig. B1 (a) describes the stress state of several points distributed on an arched differential element using a Mohr circle placed on the coordinate system.

For points A_1, A_2, and A_3 at the arched soil-layer element in Fig. 5 (a), 5 (b), and 5 (c), respectively, we have.

$$\sigma_w + c\cot\phi = (\sigma_1 + c\cot\phi)\cos^2\theta_w + (\sigma_3 + c\cot\phi)\sin^2\theta_w \tag{B1}$$

where σ_w is the horizontal earth pressure, and θ_w is the rotation angle of major principle stress σ_1.

According to geometrical relations of the Mohr's circle [Fig. 5 (a)], we have.

$$[(\sigma_w + c\cot\phi) - (\sigma_3 + c\cot\phi)]\tan\theta_w = (\sigma_w + c\cot\phi)\tan\delta \tag{B2}$$

Substituting Eq. (B.1) into Eq. (B.2), we obtain.

$$\tan\theta_w = \frac{N + \tan^2\theta_w}{N - 1}\tan\delta \tag{B3}$$

Solving Eq. (B. 3) to get.

$$\theta_w = \arctan\left(\frac{N - 1 \pm \sqrt{(N-1)^2 - 4N\tan^2\delta}}{2\tan\delta}\right) \tag{B4}$$

The points on the slip surface are at the limit state, where the Mohr circles are tangent to the Mohr-Coulomb failure line (see Fig. B1-b). Therefore, the rotation angle θ_s of the major principal stress at the slip surface can be expressed as.

$$\theta_s = \frac{\pi}{4} - \frac{\phi}{2} + \alpha = \frac{3\pi}{4} + \frac{\phi}{2} - \theta \tag{B5}$$

Appendix C. . Formulation of the log-spiral slip surface

A log-spiral function is employed to approximate the curved slip surface, which can be derived using the variational limit equilibrium method (Das and Sobhan, 2013). The equation of the log-spiral slip surface is given as.

$$r(\theta) = r_0 e^{\theta\tan\varphi} \tag{C1}$$

According to the geometric relationships given in Fig. 5 (c), the following equations can be obtained:

$$\theta_1 = \frac{\pi}{2} - \alpha_f + \phi \tag{C2}$$

$$\alpha = \frac{\pi}{2} + \phi - \theta \tag{C3}$$

where α is an angle between the tangent line at any point on the slip surface and the horizontal.

From MC failure criterion [Fig. 5 (b)], the rotation angle θ_s of major principal stress at the slip surface is given as.

$$\theta_s = \alpha + \frac{\pi}{4} - \frac{\phi}{2} \tag{C4}$$

In light of the observed results in Fig. 4 (b), we give.

$$\theta_w = \arctan\left(\frac{N - 1 + \sqrt{(N-1)^2 - 4N\tan^2\delta}}{2\tan\delta}\right) \tag{C5}$$

θ_s at the intersection point between the stationary wall and the slip surface can be calculated by the limit equilibrium state of the wall-soil interface, as below:

$$\theta_s = \pi - \theta_w \tag{C6}$$

Substituting Eqs. (C 0.2) and (B. 3) into (C. 6), we obtain.

$$\theta_2 = \frac{\varphi}{2} - \frac{\pi}{4} + \theta_w \tag{C7}$$

Further according to the geometric relationship in Fig. 5 (c), we have.

$$r_0 = \frac{B}{e^{\theta_2 \tan\phi}\cos\theta_2 - e^{\theta_1 \tan\phi}\cos\theta_1} \tag{C8}$$

Appendix D. Supplementary material

Supplementary data to this article can be found online at https://doi.org/10.1016/j.compgeo.2022.104849.

References

Anderson, D.G., 2008. Seismic analysis and design of retaining walls, buried structures, slopes, and embankments. Transportation Research Board, Washington, DC.

Cao, W., Zhang, H., Liu, T., Tan, X., 2020. Analytical solution for the active earth pressure of cohesionless soil behind an inclined retaining wall based on the curved thin-layer element method. Comput. Geotech. 128, 103851. https://doi.org/10.1016/j.compgeo.2020.103851.

Chen, F., Miao, G., Lai, F.-W., 2020. Base Instability Triggered by Hydraulic Uplift of Pit-in-Pit Braced Excavations in Soft Clay Overlying a Confined Aquifer. KSCE J. Civ. Eng. 24 (6), 1717–1730. https://doi.org/10.1007/s12205-020-1102-2.

Chen, F., Yang, J., Lin, Y., 2019. Active Earth Pressure of Narrow Granular Backfill against Rigid Retaining Wall Near Rock Face under Translation Mode. Int. J. Geomech. 19 (12), 04019133. https://doi.org/10.1061/(ASCE)GM.1943-5622.0001525.

Chen, F.-Q., Lin, Y.-J., Yang, J.-T., Huang, M., 2021. Passive Earth Pressure of Narrow Cohesionless Backfill Against Rigid Retaining Walls Rotating About the Base. Int. J. Geomech. 21 (1), 06020036. https://doi.org/10.1061/(ASCE)GM.1943-5622.0001889.

Chen, J.-J., Li, M.-G., Wang, J.-H., 2017. Active earth pressure against rigid retaining walls subjected to confined cohesionless soil. Int. J. Geomech. 17 (6), 06016041. https://doi.org/10.1061/(ASCE)GM.1943-5622.0000855.

Coulomb, C.A., 1776.. Essai sur une application des regles de maximis et minimis a quelques problemes de statique relatifs a l'architecture Mémoires Math Phys Acad. Roy Sci. 7, 343–382.

Das BM, Sobhan K., 2013. Principles of geotechnical engineering. Cengage Learn, Chapter 14: Lateral earth pressure: curved failure surface, pp. 606–609.

Deng, C., Haigh, S.K., 2020. Sand deformation mechanisms mobilised with active retaining wall movement. Géotechnique. 72 (3), 1–14. https://doi.org/10.1680/jgeot.20.P.041.

Deng, C., Haigh, S.K., 2021. Earth pressures mobilised in dry sand with active rigid retaining wall movement. Géotech. Lett. 11 (3), 202–208. https://doi.org/10.1680/jgele.20.00116.

Fan, C.-C., Fang, Y.-S., 2010. Numerical solution of active earth pressures on rigid retaining walls built near rock faces. Comput. Geotech. 37 (7), 1023–1029. https://doi.org/10.1016/j.compgeo.2010.08.004.

Fang, Y., Cheng, F., Chen, R., Fan, C., 1993. Earth pressures under general wall movements. J. Geotech. Geoenviron. Eng. 24 (2).

Fang, Y.S., Ishibashi, I., 1986. Static earth pressures with various wall movements. J. Geotech. Eng.. 112 (3), 317–333. https://doi.org/10.1061/(ASCE)0733-9410(1986)112:3(317).

Frydman, S., Keissar, I., 1987. Earth pressure on retaining walls near rock faces. J. Geotech. Eng.. 113 (6), 586–599. https://doi.org/10.1061/(ASCE)0733-9410(1987)113:6(586).

Goel, S., Patra, N.R., 2008. Effect of Arching on Active Earth Pressure for Rigid Retaining Walls Considering Translation Mode. Int. J. Geomech. 8 (2), 123–133.

Handy, R.L., 1985. The Arch in Soil Arching. J. Geotech. Eng.. 111 (3), 302–318.

Harrop-Williams, K.O., 1989. Geostatic wall pressures. J. Geotech. Geoenviron. Eng. 115 (9), 1321–1325. https://doi.org/10.1061/(ASCE)0733-9410(1985)111:3(302).

Horgan, G.J., Sarsby, R.W., 2002. The arching effect of soils over voids and piles incorporating geosynthetic reinforcement. Geosynthetics 7th ICG. 90 (5809), 523.

Jiang, M., He, J., Wang, J., Liu, F., Zhang, W., 2014. Distinct simulation of earth pressure against a rigid retaining wall considering inter-particle rolling resistance in sandy backfill. Granular Matter 16 (5), 797–814. https://doi.org/10.1007/s10035-014-0515-3.

Khatri, V.N., Kumar, J., Akhtar, S., 2017. Bearing Capacity of Foundations with Inclusion of Dense Sand Layer over Loose Sand Strata. Int. J. Geomech. 17 (10), 06017018. https://doi.org/10.1061/(ASCE)GM.1943-5622.0000980.

Krabbenhoft, K., 2018. Static and seismic earth pressure coefficients for vertical walls with horizontal backfill. Soil Dyn. Earthq. Eng. 104, 403–407. https://doi.org/10.1016/j.soildyn.2017.11.011.

Lai, F., Chen, S., Xue, J., Chen, F., 2020. New analytical solutions for shallow cohesive soils overlying trench voids under various slip surfaces. Transp. Geotech. 25, 100411. https://doi.org/10.1016/j.trgeo.2020.100411.

Lai, F., Liu, S., Li, Y., Sun, Y., 2022b. A new installation technology of large diameter deeply-buried caissons: Practical application and observed performance. Tunn. Undergr. Sp. Tech. 125, 104507.

Lai, F., Yang, D., Liu, S., Zhang, H., Cheng, Y., 2022a. Towards an improved analytical framework to estimate active earth pressure in narrow c – ϕ soils behind rotating walls about the base. Comput. Geotech. 141, 104544. https://doi.org/10.1016/j.compgeo.2021.104544.

Lai, F., Zhang, N., Liu, S., Sun, Y., Li, Y., 2021. Ground movements induced by installation of twin large diameter deeply-buried caissons: 3D numerical modeling. Acta Geotech. 16 (9), 2933–2961. https://doi.org/10.1007/s11440-021-01165-1.

Li, Z.-W., Yang, X.-L., 2019. Active earth pressure for retaining structures in cohesive backfills with tensile strength cut-off. Comput. Geotech. 110, 242–250. https://doi.org/10.1016/j.compgeo.2019.02.023.

Low, B.K., Tang, S.K., Choa, V., 1994. Arching in piled embankments. J. Geotech. Geoenviron. Eng. 120 (11), 1917–1938. https://doi.org/10.1061/(ASCE)0733-9410(1994)120:11(1917).

Lu, W., Miao, L., 2015. A simplified 2-D evaluation method of the arching effect for geosynthetic-reinforced and pile-supported embankments. Comput. Geotech. 65, 97–103. https://doi.org/10.1016/j.compgeo.2014.11.014.

Naughton, P.J., Kempton, G.T., 2005. Comparison of analytical and numerical analysis design methods for piled embankments. In Contemporary Issues in Foundation Engineering 1–10.

Ni, P., Song, L., Mei, G., Zhao, Y., 2018a. On predicting displacement-dependent earth pressure for laterally loaded piles. Soils Found. 58 (1), 85–96. https://doi.org/10.1016/j.sandf.2017.11.007.

Ni, P., Mangalathu, S., Song, L., Mei, G., Zhao, Y., 2018b. Displacement-Dependent Lateral Earth Pressure Models. J. Eng. Mech. 144 (6), 04018032. https://doi.org/10.1061/(ASCE)EM.1943-7889.0001451.

Ni, P., Mei, G., Zhao, Y., 2017. Displacement-dependent earth pressures on rigid retaining walls with compressible geofoam inclusions: physical modeling and analytical solutions. Int. J. Geomech. 17 (6), 04016132. https://doi.org/10.1061/(ASCE)GM.1943-5622.0000838.

Paik, K.H., Salgado, R., 2003. Estimation of active earth pressure against rigid retaining walls considering arching effects. Géotechnique 53 (7), 643–653.

Ukritchon, B., Keawsawasvong, S., 2016. Undrained pullout capacity of cylindrical suction caissons by finite element limit analysis. Comput. Geotech. 80, 301–311. https://doi.org/10.1016/j.compgeo.2016.08.019.

Rankine, W.J.M., 1857. On the stability of loose earth. Philos. Trans. R. Soc. Lond. 147, 9–27.

Rui, R., Ye, Y.-Q., Han, J., Zhang, L., Zhai, Y.-X., 2020. Experimental and theoretical investigations on active earth pressure distributions behind rigid retaining walls with narrow backfill under a translational mode. Int. J. Geomech. 20 (10), 04020178. https://doi.org/10.1061/(ASCE)GM.1943-5622.0001832.

Sloan, S.W., 2013. Geotechnical stability analysis. Géotechnique 63 (7), 531–571. https://doi.org/10.1680/geot.12.RL.001.

Take, W.A., Valsangkar, A.J., 2001. Earth pressures on unyielding retaining walls of narrow backfill width. Can. Geotech. J. 38 (6), 1220–1230. https://doi.org/10.1139/cgj-38-6-1220.

Terzaghi, K., 1943. Theoretical soil mechanics. John Wiley and Sons, New York.

Terzaghi, K., 1936. A fundamental fallacy in earth pressure computations. Journal of Boston Society of Civil Engineers 23 (2), 71–88.

Tschuchnigg, F., Schweiger, H.F., Sloan, S.W., 2015. Slope stability analysis by means of finite element limit analysis and finite element strength reduction techniques. Part I: Numerical studies considering non-associated plasticity. Comput. Geotech. 70, 169–177. https://doi.org/10.1016/j.compgeo.2015.06.018.

Xie, M., Zheng, J., Zhang, R., Cui, L., Miao, C., 2020. Active Earth Pressure on Rigid Retaining Walls Built Near Rock Faces. Int. J. Geomech. 20 (6), 04020061. https://doi.org/10.1061/(ASCE)GM.1943-5622.0001675.

Xie, Y., Leshchinsky, B., 2016. Active earth pressures from a log-spiral slip surface with arching effects. Géotech. Lett. 6 (2), 149–155.

Xu, L., Chen, H.-B., Chen, F.-Q., Lin, Y.-J., Lin, C., 2022. An experimental study of the active failure mechanism of narrow backfills installed behind rigid retaining walls conducted using Geo-PIV. Acta Geotech. https://doi.org/10.1007/s11440-021-01438-9.

Xu, S.-Y., Lawal, A.I., Shamsabadi, A., Taciroglu, E., 2019. Estimation of static earth pressures for a sloping cohesive backfill using extended Rankine theory with a composite log-spiral failure surface. Acta Geotech. 14 (2), 579–594.

Yang, M., Tang, X., 2017. Rigid Retaining Walls with Narrow Cohesionless Backfills under Various Wall Movement Modes. Int. J. Geomech. 17 (11), 04017098. https://doi.org/10.1061/(ASCE)GM.1943-5622.0001007.

Yang, X.-L., Huang, F., 2011. Collapse mechanism of shallow tunnel based on nonlinear Hoek-Brown failure criterion. Tunn. Undergr. Space Technol. 26 (6), 686–691. https://doi.org/10.1016/j.tust.2011.05.008.

Yang, X.-L., Yin, J.-H., 2004. Slope Stability Analysis with Nonlinear Failure Criterion. J. Eng. Mech. 130 (3), 267–273. https://doi.org/10.1061/(ASCE)0733-9399(2004)130:3(267).